LASER MATERIALS AND TECHNOLOGY RESEARCH CENTER

OF GENERAL PHYSICS INSTITUTE

ISTC project No 1697p

Excitation of molecular gas high overtones

by tuneable and solid state lasers

Final report

Moscow

September 2001

REPORT DOCUMENTATION PAGE

Form Approved OMB No. 0704-0188

Public reporting burden for this collection of information is estimated to average 1 hour per response, including the time for reviewing instructions, searching existing data sources, gathering and maintaining the data needed, and completing and reviewing the collection of information. Send comments regarding this burden estimate or any other aspect of this collection of information, including suggestions for reducing the burden, to Department of Defense, Washington Headquarters Services, Directorate for Information Operations and Reports (0704-0188), 1215 Jefferson Davis Highway, Suite 1204, Arlington, VA 22202-4302. Respondents should be aware that notwithstanding any other provision of law, no person shall be subject to any penalty for failing to comply with a collection of information if it does not display a currently valid OMB control number.
PLEASE DO NOT RETURN YOUR FORM TO THE ABOVE ADDRESS.

1. REPORT DATE *(DD-MM-YYYY)*	2. REPORT TYPE	3. DATES COVERED *(From – To)*
19-10-2001	Final Report	01/04/2000 - 19-Oct-01

4. TITLE AND SUBTITLE

Excitation of molecular gas high overtones by tunable and solid state lasers

5a. CONTRACT NUMBER
ISTC Registration No: 1697

5b. GRANT NUMBER

5c. PROGRAM ELEMENT NUMBER

6. AUTHOR(S)

Professor Tasoltan Tazretovich Basiev

5d. PROJECT NUMBER

5d. TASK NUMBER

5e. WORK UNIT NUMBER

7. PERFORMING ORGANIZATION NAME(S) AND ADDRESS(ES)
General Physics Institute of the Russian Academy of Sciences
38 Vavilov St
Moscow 117942
Russia

8. PERFORMING ORGANIZATION REPORT NUMBER

N/A

9. SPONSORING/MONITORING AGENCY NAME(S) AND ADDRESS(ES)

EOARD
PSC 802 BOX 14
FPO 09499-0014

10. SPONSOR/MONITOR'S ACRONYM(S)

11. SPONSOR/MONITOR'S REPORT NUMBER(S)
ISTC 00-7002

12. DISTRIBUTION/AVAILABILITY STATEMENT

Approved for public release; distribution is unlimited.

13. SUPPLEMENTARY NOTES

14. ABSTRACT

This report results from a contract tasking General Physics Institute of the Russian Academy of Sciences as follows:
The contractor will investigate the applicability of external and intracavity optical pumping of molecular gas cells by tunable color center lasers and by solid state crystalline lasers to produce a tunable mid-IR laser oscillating on vibrational transitions of the molecule.

15. SUBJECT TERMS
EOARD, Physics, Optics

16. SECURITY CLASSIFICATION OF:			17. LIMITATION OF ABSTRACT	18, NUMBER OF PAGES	19a. NAME OF RESPONSIBLE PERSON
a. REPORT UNCLAS	b. ABSTRACT UNCLAS	c. THIS PAGE UNCLAS	UL	60	Alexander J. Glass, Ph.D.
					19b. TELEPHONE NUMBER *(Include area code)* +44 02 7514-4953

Standard Form 298 (Rev. 8/98)
Prescribed by ANSI Std. Z39-18

Content

1. Numerical modeling of the optically pumped mid-infrared molecular lasers

Introduction

The optically pumped mid-infrared molecular lasers were studied by the numerical modeling methods. The intra-cavity and external-cavity pumping schemes were investigated. The mathematical description of the optical pumping was based on a standard approach of the rate equations for laser active mediums. The laser radiation was modeled in terms of photons flow density. The laser beams were considered to be uniform. To model the laser beams propagation in the active medium, the transfer equations were used.

The description of laser medium models is presented in the first part of the report. The molecular gas medium model (section 1.1.1) was built in approximation of the instant R-T relaxation, the V-T relaxation was neglected.

The optical pumping of the gas medium by the $LiF : F_2^-$ color-center laser and by GGG:Nd laser was studied. For the modeling of the $LiF : F_2^-$ color-center crystal, the standard two-level approximation was used (section 1.1.2). The coherent longitudinal pumping of the color-center crystal was considered. The model of GGG:Nd crystal was also built on a basis of a two level scheme (section 1.1.3). The GGG:Nd crystal rate equations were written out for the case of a flash lamp pumping and a Q-switched laser cavity.

The spectral characteristics of a pump laser is an important parameter of the optically pumped molecular laser. Therefore, the pump laser radiation was considered to consist of multiple frequency components (section 1.1.4). Such an approach allows one to simulate the narrowing of the pump laser spectrum in the dispersive laser cavity (cavity with a diffraction grating for $LiF : F_2^-$ laser or intra-cavity etalon for GGG:Nd laser).

The numerical modeling results are presented in part 2 ($LiF : F_2^-$ pumping) and part 3 (GGG:Nd pumping) of the report. The structure of the both parts is similar. In each part, the basic parameters of the molecular laser are given in introduction, then the description of laser cavity models and the modeling results are follow.

The main results of the theoretical study are presented in conclusion.

1.1. Model of the molecular gas medium pumped by the solid state laser

1.1.1. Simplified model of the molecular gas

The gas medium energy levels scheme is shown in the fig. 1.1. The spectrum consist of the vibronic energy bands V0, V1, V2, … Each vibronic band contains the rotational sublevels J0, J1, J2, …The pumping of the medium through the second (V0→V2) or the third (V0→V3) overtone transitions was modeled, therefore the upper vibronic levels were not taken into account.

The optical transitions in the gas medium occur with simultaneous shift of the vibronic quantum number $\Delta V = 1, 2,...$ and the rotational quantum number $\Delta J = \pm 1$:

$$M(V,J) \rightarrow M(V',J \pm 1) \pm h\nu \qquad (1.1.)$$

The molecular collisions cause the radiation-less relaxations in the medium: rotational relaxation without the modification of the vibronic quantum number (R-T relaxation)

$$M(V,J) + M' \rightarrow M(V,J') + M''; \qquad (1.2.)$$

collisions with simultaneous modification of the vibronic number of two molecules (V-V relaxation)

$$\begin{aligned} M(V=2) + M(V=0) &\leftrightarrow \\ M(V=1) + M(V=1) &\pm \Delta E_{V-V} \end{aligned} \qquad (1.3.)$$

and

$$\begin{aligned} M(V=3) + M(V=0) &\leftrightarrow \\ M(V=2) + M(V=1) &\pm \Delta E_{V-V} \end{aligned}; \qquad (1.4.)$$

collisions with the energy transfer from the excited molecular vibronic level to the translation degrees of freedom of the ground vibronic level (V-T relaxation)

$$\begin{aligned} M(V=1) + M(V=0) &\rightarrow \\ M(V=0) + M(V=0) &+ \Delta E_{V-T} \end{aligned}. \qquad (1.5.)$$
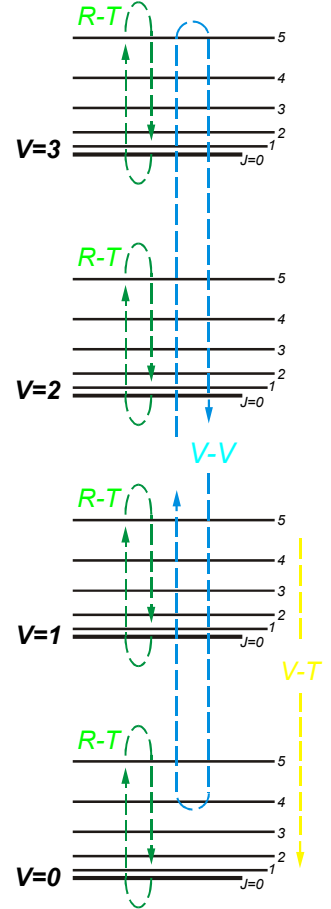

Fig. 1.1

The fastest relaxation process is the R-T relaxation. The typical R-T relaxation rate k_{R-T} is about $10^{-10}\ cm^3/sec$. The V-V relaxation is approximately hundred times slower $k_{V-T} \sim 10^{-12}\ cm^3/sec$. The slowest one is the V-T relaxation $k_{V-T} \sim 10^{-14} - 10^{-17}\ cm^3/sec$. For the gas pressure about 10 torr and the room temperature, the above rates put the following relaxation times: $\tau_{R-T} \sim 10^{-8}\ sec$, $\tau_{V-V} \sim 10^{-6}\ sec$, $\tau_{V-T} \sim 10^{-4} - 10^{-2}\ sec$ [i].

The significant difference in the relaxation reactions rates allowed one to simplify the molecular gas medium model: the R-T relaxation was considered as instant and the V-T relaxation was neglected. Thus, the molecular gas medium was described by the simplified energy levels diagram, which is shown in the fig. 1.2. The vibronic levels V1, V2, V3 of the molecule are considered to be structure-less and equidistant. The lower vibronic state consist of the two sublevels, V0 and V0′. The particles distribution between the V0 and V0′ sublevels is thermal due to the very fast R-T relaxation.
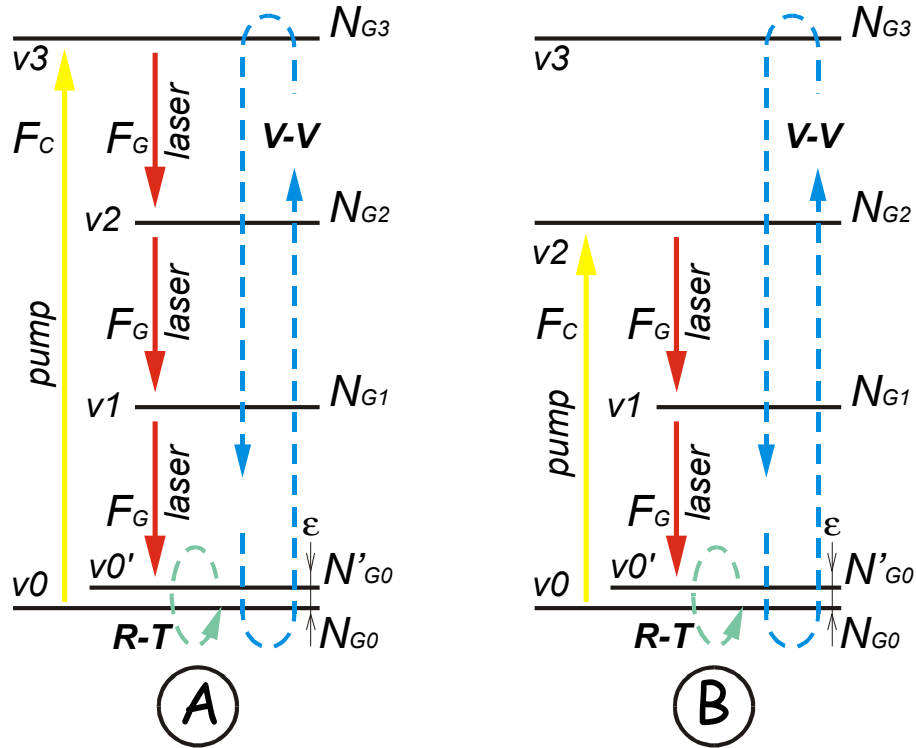

Fig. 1.2

i J.E. McCord, A.A. Jonin, S.P. Philips, P.G. Crowell, A.I. Lampson, J.K. McIver, A.J.W.Brown, and G.D. Hager "Frequency-tunable optically pumped carbon monoxide laser" IEEE Journal of Quantum Electronics, vol. 36, No 9, p. 1041 (2000)

The absorption of the pump radiation causes transitions from the lower state V0 to the upper laser state (state V3 for the pumping in to the third overtone, fig. 1.2a, or state V2 for the pumping into the second overtone, fig. 1.2b). Decay of the excited molecules goes through the sequence of spontaneous and stimulated transitions between levels V3, V2, V1 and V0′ and due to the radiation-less V-V relaxation. If the V-V relaxation does not taken into account directly, then the rate equations for the gas medium could be written in the following form:

$$\begin{cases} \partial N_{G3}/\partial t = (N_{G0} - N_{G3})\int \tilde{\sigma}_G(\nu)f_C(\nu)d\nu + N_{G2}\sigma_G F_G - N_{G3}\sigma_G F_G - N_{G3}/\tau_G \\ \partial N_{G2}/\partial t = N_{G3}\sigma_G F_G + N_{G3}/\tau_G + N_{G1}\sigma_G F_G - 2N_{G2}\sigma_G F_G - N_{G2}/\tau_G \\ \partial N_{G1}/\partial t = N_{G2}\sigma_G F_G + N_{G2}/\tau_G + N'_{G0}\sigma_G F_G - 2N_{G1}\sigma_G F_G - N_{G1}/\tau_G \\ N'_{G0}/N_{G0} = exp(-\varepsilon/kT) \\ \quad N_G = N_{G0} + N'_{G0} + N_{G1} + N_{G2} + N_{G3} = const \end{cases} \quad (1.6.)$$

for the third overtone pumping and

$$\begin{cases} \partial N_{G2}/\partial t = (N_{G0} - N_{G2})\int \tilde{\sigma}_G(\nu)f_C(\nu)d\nu + N_{G1}\sigma_G F_G - N_{G2}\sigma_G F_G - N_{G2}/\tau_G \\ \partial N_{G1}/\partial t = N_{G2}\sigma_G F_G + N_{G2}/\tau_G + N'_{G0}\sigma_G F_G - 2N_{G1}\sigma_G F_G - N_{G1}/\tau_G \\ N'_{G0}/N_{G0} = exp(-\varepsilon/kT) \\ \quad N_G = N_{G0} + N'_{G0} + N_{G1} + N_{G2} + N_{G3} = const \end{cases} \quad (1.7.)$$

for the second overtone pumping. In the eq. (6) and eq. (7) the following designations were used: N_{Gi} – gas medium levels populations [cm^{-3}]; $f_C(\nu)$ – pump radiation photons flow spectral density [$sec^{-1}cm^{-2}Gz^{-1}$]; F_G – gas medium emission photons flow density [$sec^{-1}cm^{-2}$]; σ_G – effective cross-section of stimulated transitions at the gas emission wavelength [cm^2]; τ_G – characteristic time of the spontaneous transitions at the gas emission wavelength [sec]; $\tilde{\sigma}_G(\nu)$ – the gas medium absorption contour [cm^2]. The gas absorption was approximated by Gauss function:

$$\sigma_G(\nu - \nu_0) = \sigma_G^{(0)} exp\left[-\left(\frac{\nu - \nu_0}{\Delta\nu_G/2}\right)^2\right] \quad (1.8.)$$

there ν_0 is the line center, $\Delta\nu_G$ – is the absorption line-width.

To simulate the V-V relaxation in the gas medium, reactions (3) and (4) have been taken into account. To have an upper-estimation of the V-V relaxation effect, the reactions were considered unidirectional: V0 → V1 and V2 → V1 transitions for the reaction (3); V0 → V1 and V3 → V2

transitions for the reaction (4). The both reactions rates were considered equal. Thus, the modified rate equations for the gas medium with V-V relaxation were:

$$\begin{cases} \partial N_{G3}/\partial t = \ldots - N_{G3}N_{G0}k_{V-V} \\ \partial N_{G2}/\partial t = \ldots - N_{G2}N_{G0}k_{V-V} + N_{G3}N_{G0}k_{V-V} \\ \partial N_{G1}/\partial t = \ldots + 2N_{G2}N_{G0}k_{V-V} + N_{G3}N_{G0}k_{V-V} \end{cases} \qquad (1.9.)$$

where dotes denote the optical transitions (are the same as in eq. (6) or eq. 7)).

1.1.2. Rate equations for the $LiF : F_2^-$ color-center crystal

The $LiF : F_2^-$ color center crystal laser medium was modeled on the basis of the following assumptions:

o   two-level approximation for the laser medium

o   coherent optical pumping

o   longitudinal pumping scheme

The energy diagram of the $LiF : F_2^-$ color center crystal is shown on the fig. 1.3. The following processes were taken into account: absorption and stimulated emission at the pump radiation wave-length (C1); absorption and stimulated emission of the color center laser radiation (C2); spontaneous emission at the color center laser wavelength (C3). Thus, the rate equations for the energy levels populations in the $LiF : F_2^-$ crystal could be written out in the form:

Fig. 1.3

$$\begin{cases} \partial N_{C1}/\partial t = \left(N_{C0}\sigma_P^{(01)} - N_{C1}\sigma_P^{(10)}\right)F_P + \\ \qquad + \left(N_{C0}\sigma_C^{(01)} - N_{C1}\sigma_C^{(10)}\right)F_C - N_{C1}/\tau_C \quad (1.10.) \\ N_C = N_{C1} + N_{C0} = const \end{cases}$$

where N_{C0} and N_{C1} are the lower and upper laser levels populations [cm^{-3}]; N_C - the total concentration of the active color centers in the crystal [cm^{-3}]; F_P – pump radiation photons flow intensity [sec^{-1}cm^{-2}]; F_C – color center laser radiation photons flow intensity
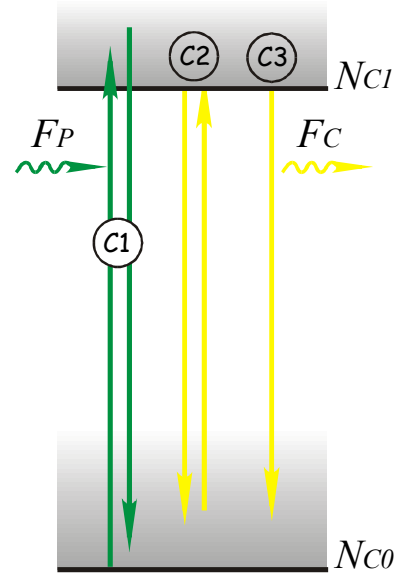

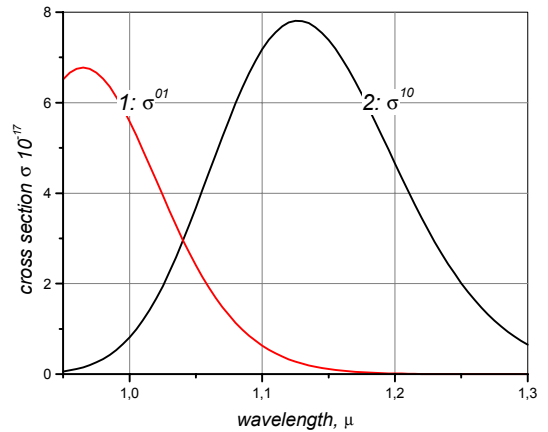*Fig. 1.4*

[sec^{-1}cm^{-2}]; $\sigma_P^{(01)}$ and $\sigma_P^{(10)}$ - the effective cross-sections of absorption and stimulated emission at the pump wavelength [cm^2]; $\sigma_C^{(01)}$ and $\sigma_C^{(10)}$ – the effective cross-sections of absorption and stimulated emission at the color center laser wavelength [cm^2]; τ_C - the color center crystal spontaneous luminescence time [sec]. The spectral behaviors of the absorption and emission effective cross-sections for the $LiF : F_2^-$ crystal are shown at the fig. 1.4. Typical concentration of the color centers in the crystal is equal approximately 3×10^{16} cm^{-3}. The characteristic time of the color-centers spontaneous decay at the room temperature is about 55 nsec.

1.1.3.   Rate equations for the GGG:Nd laser crystal

The basic assumptions for the GGG:Nd laser medium modeling were following:

o   two-level approximation for the laser medium

o   lamp pumping

o   Q-switched laser cavity

Energy levels diagram of the GGG:Nd crystal is shown on the fig. 1.5. The following processes in the GGG:Nd crystal were taken into account: stimulated absorption and emission at the pump wavelength (process A at the fig. 1.5); stimulated and spontaneous transitions at the lasing wavelength (process B). Radiation-less relaxation between the levels 3-2 and 1-0 (process C) was considered instant, relaxation between the levels 3-0 (process D) was neglected. The following rate equation for the crystal was used:
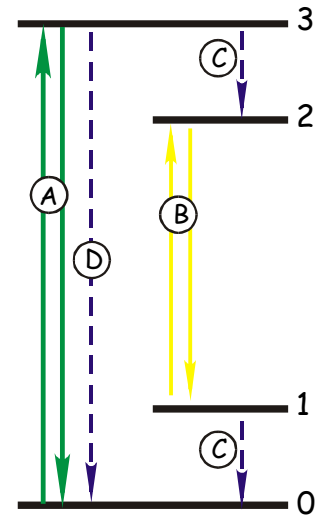

Fig. 1.5

$$\frac{\partial N_C}{\partial t} = -\left(W_P + W_C + \frac{1}{\tau_{21}}\right)N_C + NW_P \qquad (1.11.)$$

there N is a concentration of the active centers in the crystal; N_C is the energy levels 2 and 1 populations difference [cm^{-3}]; W_P is the pump transitions rate [s^{-1}]; W_C is the laser transitions rate [s^{-1}]; $1/\tau_{21}$ is the spontaneous transitions rate in the lasing channel [s^{-1}]. The approximation of the instant Q-switching was used. Therefore the final form of the rate equation was

$$\frac{\partial N_C}{\partial t} = -\frac{N_C - N_{C0}}{\tau_{21}} - NW_C = -\frac{N_C - N_{C0}}{\tau_{21}} - N_C \int f_C(v)\sigma_C(v)dv \qquad (1.12.)$$

there $f_C(\nu)$ is a spectral distribution of a photons flow density of the GGG:Nd laser emission [cm^{-2}sec^{-1}Hz^{-1}]; $\sigma_C(\nu)$ is a GGG:Nd luminescence contour[i] [cm^2]. N_{C0} is the initial laser medium population inversion before the Q-switching.

1.1.4. *Model of the multiple longitudinal modes emission of the solid state pump laser*

The particular problem of the optically pumped molecular lasers is the spectrally narrow absorption of the gas medium. Therefore, for the effective intra-cavity pumping of the gas medium by the color-center laser radiation the dispersive cavity at the pump wavelength should be used. The fig. 1.6 explains how the narrowing of the pump laser emission was modeled. The pump laser spectrum consist of a several longitudinal modes The number of lasing modes depends on the intra-cavity frequency selector band-width. In this way could be simulated the single longitudinal mode pumping as well as multiple modes pumping

Fig. 1.6

---

i   The narrowing of the GGG:Nd laser radiation by the intra-cavity etalon was simulated by the adjustment of the luminescence contour band-width.

1.2. The optical pumping of the molecular laser by $LiF : F_2^-$ color-center laser

1.2.1. Introduction

The schematic of the laser system was modeled shown at the fig. 1.7. The laser consist of the $LiF : F_2^-$ color center crystal C, the gas cell G, the cavity mirrors M1 and M2 and the frequency selector S. The pump source of the system is the radiation of Nd:YAG laser. The pump pulse initiates generation of the color center laser (radiation wavelength 1.18 μ) which pumps the gas medium (radiation wavelength ~4 μ). The major parameters of the laser system are following:

- Primary pump (Nd:YAG laser)

  o *wavelength* .... *1.06 μ*
  o *pulse energy* .... *100 mJ*
  o *pulse duration* .... *10 ns*

- Molecular pump ($LiF : F_2^-$ laser)

  o *wavelength* .... *1.18 μ*
  o *active crystal length* .... *8 cm*
  o *frequency selector band-width 1 – 10 GHz*

- Molecular laser (HCl laser)

  o *wavelength* .... *≈4 μ*
  o *pump transition* .... *V0 → V3*
  o *gas cell length* .... *10 - 40 cm*
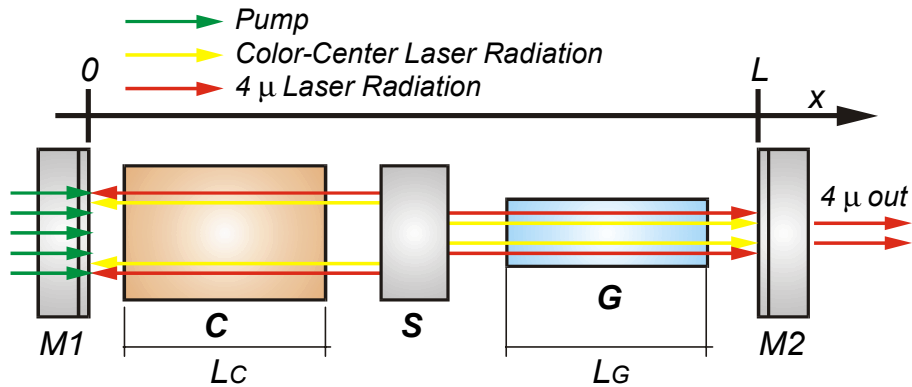

Fig. 1.7

o   *gas absorption line-width ..... 0.5 GHz*

The secondary parameters of the laser system are shown in the table below:

PARAMETER	DESIGNATION	VALUE	UNITS
laser beam cross-section in the color center crystal	S_C	*0,1*	*cm²*
color centers concentration	N_C	3×10^{16}	cm^{-3}
absorption/emission effective cross-section of the color center crystal at the pump laser wavelength	$\dfrac{\sigma_P^{01}}{\sigma_P^{10}}$	$\dfrac{1.9\times10^{-17}}{4.5\times10^{-17}}$	*cm²*
absorption/emission effective cross-section of the color center crystal at the color center laser wavelength (1.18 μ)	$\dfrac{\sigma_C^{01}}{\sigma_C^{10}}$	$\dfrac{5.6\times10^{-17}}{0.03\times10^{-17}}$	*cm²*
characteristic time of spontaneous transitions in color center crystal	τ_C	*50*	*nsec*
laser beam cross-section in the gas cell	S_G	*0,01*	*cm²*
gas molecules concentration	N_G	5×10^{17}	cm^{-3}
absorption/emission effective cross-section of the gas medium at the pump wavelength	$\widetilde{\sigma}_G$	1×10^{-20}	*cm²*
absorption/emission effective cross-section of the gas medium at the purposeful wavelength (4 μ)	σ_G	1×10^{-15}	*cm²*

The first part of this section contains the description of the laser system model. Then, the results of the modeling for the gas medium without V-V relaxation are presented. Finally, the influence of V-V relaxation at the laser system performance is discussed.

1.2.2.   *The laser cavity model*

The three types of radiation are pass through the cavity (see fig. 1.7): the pump radiation (wavelength λ_P), color center laser radiation (wavelength λ_C) and the gas medium radiation (wavelength λ_G). The pump radiation comes to the cavity through the dichroic mirror M1. The color center laser radiation which appears in the cavity drives up inversion and laser generation at the gas medium. The gas medium emission escapes the cavity through the partially transparent mirror M2. The frequency selector S have a two functions, firstly, it narrowes the color center laser generation spectrum to necessary width, secondary it works as a beam expander to reach

required color center laser radiation intensity in the gas cell. It should be noted that such an optical element could be realized by the diffraction grating in the grazing incidence mounting.

The basis of the laser system model is the rate equations (6) for the gas medium pumped via third overtone transition and the rate equations (10) for the color-center crystal. The approximations have been used for the active mediums modeling are discussed in the previous section.

On the basis of presented models of the active mediums and laser cavity we can write out the transfer equations for the radiation

- *Pump radiation*

$$
\begin{cases}
\left(\dfrac{1}{c}\dfrac{\partial}{\partial t} + \dfrac{\partial}{\partial x} \right) F_P = -\left(N_{C0}\sigma_P^{(01)} - N_{C1}\sigma_P^{(10)} \right) F_P - k_P F_P & x \in LiF : F_2^- \\[2mm]
\left(\dfrac{1}{c}\dfrac{\partial}{\partial t} + \dfrac{\partial}{\partial x} \right) F_P = 0 & x \notin LiF : F_2^-
\end{cases}
\tag{1.13.}
$$

- *Color center laser radiation*

$$
\begin{cases}
\left(\dfrac{1}{c}\dfrac{\partial}{\partial t} \pm \dfrac{\partial}{\partial x} \right) f_C^\pm = \left(N_{C1}\sigma_C^{(10)} - N_{C0}\sigma_C^{(01)} \right) f_C^\pm + \omega_C N_{C1}/\tau_C - k_C f_C^\pm & x \in LiF : F_2^- \\[2mm]
\left(\dfrac{1}{c}\dfrac{\partial}{\partial t} \pm \dfrac{\partial}{\partial x} \right) f_C^\pm = -\left(N_{G0} - N_{G3} \right)\widetilde{\sigma}_G(\nu) f_C^\pm & x \in gaz\ cell
\end{cases}
\tag{1.14.}
$$

- *IR laser radiation*

$$
\begin{cases}
\left(\dfrac{1}{c}\dfrac{\partial}{\partial t} \pm \dfrac{\partial}{\partial x} \right) F_G^\pm = \left(N_{G3} - N'_{G0} \right)\sigma_G F_G^\pm + \omega_G \left(N_{G3} + N_{G2} + N_{G1} \right)/\tau_G & x \in gaz\ cell \\[2mm]
\left(\dfrac{1}{c}\dfrac{\partial}{\partial t} \pm \dfrac{\partial}{\partial x} \right) F_G^\pm = 0 & x \notin gaz\ cell
\end{cases}
\tag{1.15.}
$$

there factor k_λ specify the parasitic absorption of the radiation in the $LiF : F_2^-$ crystal at the wavelength λ and factor ω_λ specify the fraction of spontaneously emitted photons which initiate the laser generation.

For the solution of the rate equations (6, 10) and the transfer equations (13, 14, 15) it is necessary to complete the system by the initial conditions and the boundary conditions

o *Initial conditions*

$$f_C^\pm(x, t=0) = 0$$
$$F_G^\pm(x, t=0) = 0$$
$$N_{G1} = N_{G2} = N_{G3} = 0$$
$$N_{C1} = 0$$

(1.16.)

o   *Boundary condition for the pump radiation (at the input end of the LiF : F_2^- crystal)*

$$F_P(x = x_{M1}, t) = \frac{\mathbf{E}}{\sqrt{\pi} S_C t_P} exp\left[-\frac{(t - 4t_P)^2}{t_P^2} \right]$$

(1.17.)

there $\mathbf{E}$ – pump pulse energy and t_P – pump pulse duration.

o   *Boundary conditions for the color center and mid-IR laser radiation (at the cavity mirrors)*

$$f_C^+(x = x_{M1}, t) = (1 - \alpha_C^{(M1)}) f_C^-(x = x_{M1}, t)$$
$$F_G^+(x = x_{M1}, t) = (1 - \alpha_G^{(M1)}) F_G^-(x = x_{M1}, t)$$
$$f_C^-(x = x_{M2}, t) = (1 - \alpha_C^{(M2)}) f_C^+(x = x_{M2}, t)$$
$$F_G^-(x = x_{M2}, t) = (1 - \alpha_G^{(M2)} - T_G^{(M2)}) F_G^+(x = x_{M2}, t)$$

(1.18.)

there $\alpha_\lambda^{(M1)}$ and $\alpha_\lambda^{(M2)}$ is a loss factors of the mirrors at the corresponding wavelength and $T_G^{(M2)}$ is the transmission factor of the output mirror *M2* in IR region.

o   *Additional conditions at the frequency selector S*

$$S_G f_C^+(x = x_S^+, t, \nu) = T^{(S)}(\nu) S_C f_C^+(x = x_S^-, t, \nu)$$
$$S_C f_C^-(x = x_S^-, t, \nu) = T^{(S)}(\nu) S_G f_C^-(x = x_S^+, t, \nu)$$

(1.19.)

there S_C and S_G, is the color center laser beam cross-section in the *LiF : F_2^-* crystal and in the gas cell respectively and factor $T^{(S)}(\nu)$ is the spectral profile of the selector transmission. Let's assume that the selector line has Gauss profile

$$T^{(E)}(\nu - \nu_0) = exp\left[-\left(\frac{\nu - \nu_0}{\Delta\nu_C / 2} \right)^2 \right]$$

(1.20.)

there ν_0 – central frequency of the selector and $\Delta\nu_C$ – transmission line-width. This system of partial differential equations could be solved numerically.

1.2.3.   *Simulation results for simplified model of V-V relaxation*

Influence of the gas medium parameters at the efficiency of laser system

The main characteristics of the gas medium are: effective cross-section of the gas absorption ($\tilde{\sigma}_G$); effective cross-section of the laser transitions   between the vibronic levels V3 – V2 – V1 – V0 (σ_G); characteristic lifetime of spontaneous transitions at the gas emission wavelength (τ_G); energy gap between lower laser levels V0 and V0′ (ε).

Fig. 1.8

One of the specific features of the molecular medium is a significant difference between the pump absorption cross-section $\tilde{\sigma}_G \approx 10^{-20}$ cm^2 and laser transitions cross-section $\sigma_G \approx 10^{-15}$ см^2. Our calculations have shown that such a disproportion makes the efficiency of the intra-cavity pumping depending poorly on the value of mid-infrared emission effective cross-section σ_G. As an example at the fig. 1.8 shown the typical behavior of the system output energy as a function of σ_G effective cross-section value. For horizontal axis of the plot the logarithmic scale was used. Calculations were made for $\Delta\nu_C$ = 4 GHz frequency selector transmission band width. Easy to see, that the system output became almost constant if the value of σ_G cross-section exceeds 10^{-17} см^2 (σ_G to $\tilde{\sigma}_G$ ratio exceeds 10^3). Thus, the
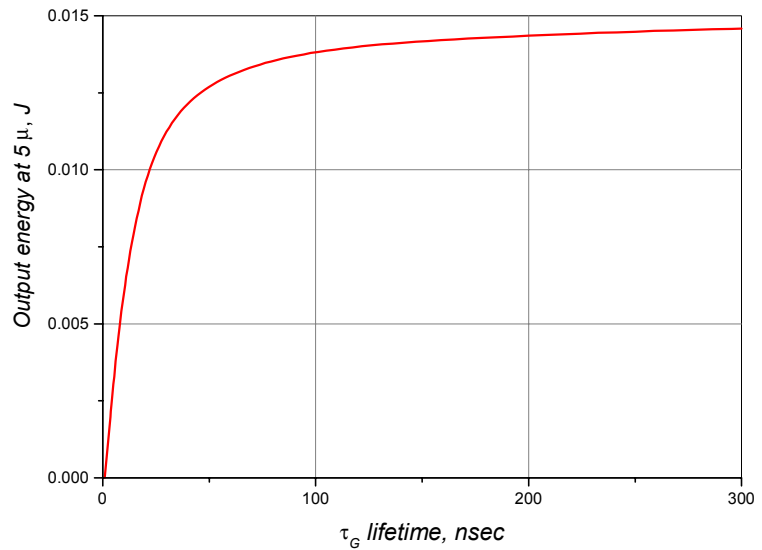

Fig. 1.9

"bottle neck" of the gas medium optical pumping process is the low rate of the pumping transitions. On the other hand parameters of the stimulated transitions at the laser wavelength does not affect on the efficiency of the system as a whole.

Fig. 1.10

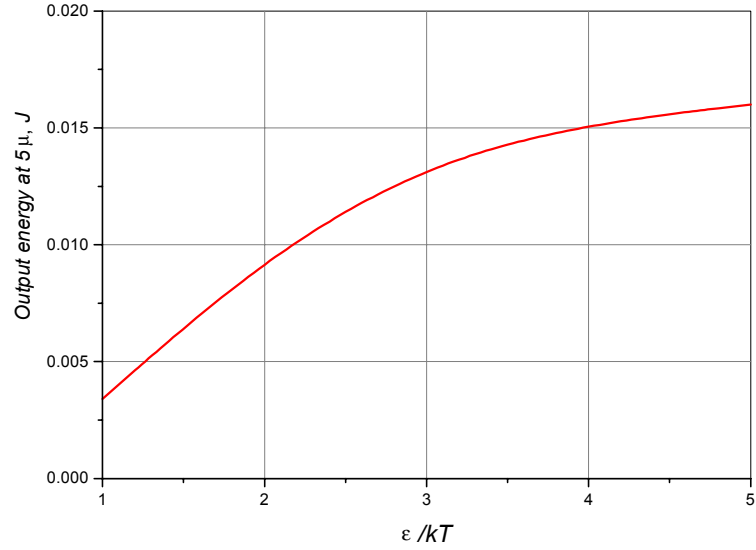Second important parameter of the gas medium is the rate of the spontaneous luminescence and radiation-less relaxation in the system. In the first approximation both these processes was considered though the factor τ_G (relaxation lifetime). On the fig. 1.9 is shown the behavior of the laser system output energy as a function of lifetime τ_G. From the picture is follows, that the relaxation processes became significant if τ_G is less than 50 nsec. For the further calculations the lifetime τ_G was chosen to be equal 55 nsec [i]. However, for more correct modeling and optimization of the gas cell is important to take into account rigorously the process of V-V relaxation.

At the fig. 1.10 is shown the behavior of the laser system output efficiency as a function of the energy gap ε between two lowest laser levels (levels V0 and V'0 on the fig. 1.2). The efficiency of the system falls rapidly with decrease of parameter ε/kT. For the further calculations $\varepsilon/kT = 3$ was used.

---

[i] At the room temperature such a decay time corresponds to the gas pressure about 200 torr ($N_G \approx 6 \times 10^{18}\ cm^{-3}$). Thus, in the gas pressure range we are considering, the influence of the V-V relaxation was over-estimated.

Optimization of the gas cell parameters

The main parameters of the gas cell are the concentration of the gas molecules in the cell and length of the cell. The optimization of the cell parameters was carried out in the approximation of constant relaxation rate in the gas medium. On the fig. 1.11 and fig. 1.12 are shown the efficiency of the laser generation as a function of the spectral selector transmission band-width $\Delta\nu_C$ (which determines the color center laser emission line-width).

Calculations were made for different molecules concentrations in the cell N_G (see graph legends) and different cell lengths L_G (L_G = 10 cm for fig. 1.11 and L_G = 30 cm for fig. 1.12). Obviously, the efficiency of the system goes down with increase of the pump laser line-width. At the narrow-line pumping ($\Delta\nu_C$ < 2 GHz) the output energy of the system is enough sensitive to the gas molecules concentration. For the broad-band pumping influence of the concentration became less significant. For the long-length cell (fig. 1.12) influence of the concentration is minimal, however the pump to output conversion efficiency remains high enough

Thus, for the given pump laser line-width the optimal relation between cell length and molecules concentration could be
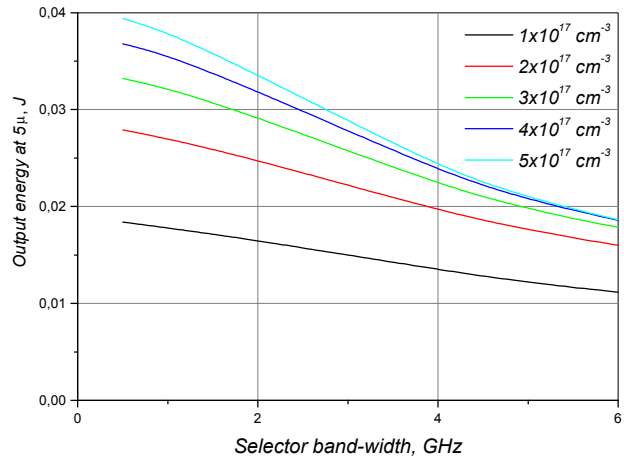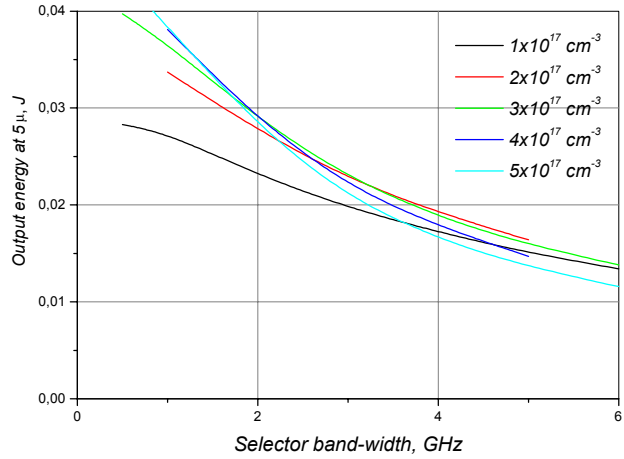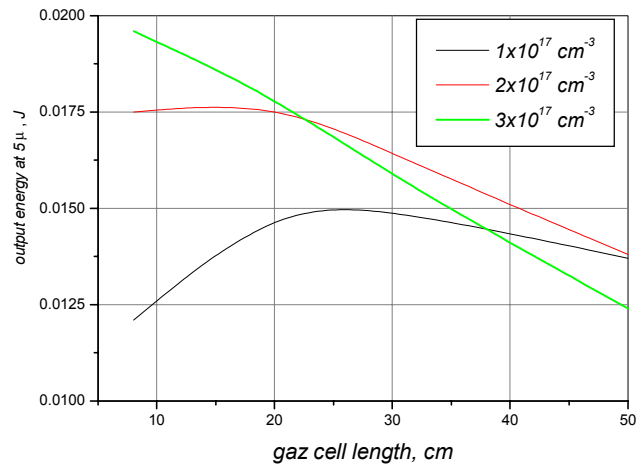

Fig. 1.11

Fig. 1.12

Fig. 1.13

determined. At the fig. 1.13 are shown the results of such optimization for Δv = 4 GHz. With rise of the concentration the optimal cell length decreases rapidly and behavior of the laser efficiency as a function of the cell length became more sharp.

Influence of the cavity parameters at the laser system performance

Let's consider the influence of the cavity losses at the color center laser wavelength and at the gas laser emission wavelength to the output characteristics of the system. The calculations in this section were made for 20 cm long gas cell and 3×10^{17} gas molecules concentration.

On the fig. 1.14 are shown the behaviors of the laser output energy as a function of parasitic losses in the laser cavity. Such a losses are caused by the cavity optics imperfectness, parasitic absorption in the color center crystal etc. Calculations were carried out for different band-widths of the intra-cavity frequency selector (see graph legend). One can see that the efficiency of the laser operation falls rapidly with increase of the losses at the color center laser wavelength. Thus, the high Q-factor of the color center laser cavity are rather important for the effective intra-cavity optical pumping of the gas medium.

Requirements to the cavity quality at the gas laser operation wavelength are not as high. On the fig. 1.15 shown the output laser efficiency as a function of the cavity
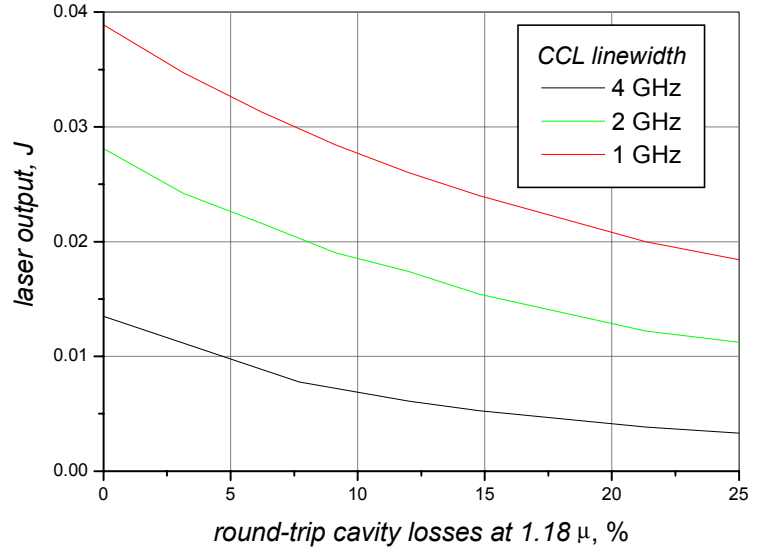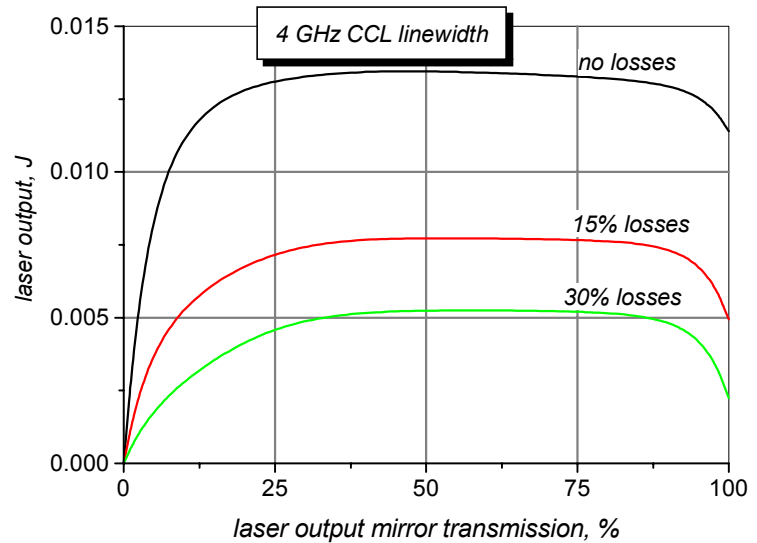

Fig. 1.14

Fig. 1.15

mirror transmission in the 4 μ wavelength region (output mirror M2 on the fig. 1.7). Easy to see that the laser efficiency remains constant while the output mirror transmission alters from 20% to the 80%. However, the alteration of the cavity feedback at the molecular laser operation wavelength allows to adjust the temporal shape of the output pulse. On the fig. 1.16 are shown the laser pulses for different transmissions of the output mirror. The

Fig. 1.16

picture allows to conclude, that 75% transmission looks optimal because it provide more uniform and short laser pulse with higher peak power.
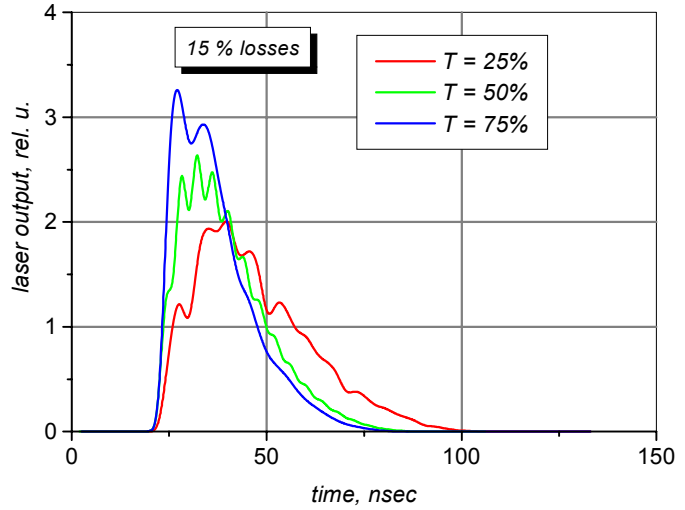
* * *

The results presented in this section allow to establish the following requirements to the cavity parameters of the laser system.

o The single-longitudinal-mode operation of the pump laser is important for the effective lasing in mid-infrared. However, the molecular laser operation is possible also with double or triple longitudinal-modes pumping. The use of multiple modes pumping reduces several times the molecular laser output.

o We consider the 30% reduction of the molecular laser efficiency due to the parasitic losses in the laser cavity as a reasonable limit for the experimental realization of the intra-cavity pumped molecular laser. Our calculations show that the use of high Q-factor cavity at the color-center laser wavelength is essential for effective lasing in mid-IR. The 10% cavity-round-trip losses at the pump laser wavelength reduce the mid-IR laser output by 30% and the 20% losses reduce output by 50%.

o The cavity parameters in mid-IR are secondary. Adjustment of the cavity Q-factor at the molecular emission wavelength allows to improve the temporal characteristics of the laser output (increase the pulse peak power by shortening of the pulse duration) but does not affect strongly at the laser efficiency.

1.2.4.   Simulation results for accurate model of V-V relaxation

To take into account the V-V relaxation more accurately the modified rate equations for molecular gas medium were used (see. eq. (6) and eq. (9)) [i]. The equations describing the laser cavity model (transfer equations (13, 14, 15) and boundary conditions (16, 17, 18, 19)) were the same.

At the fig. 1.17 and fig. 1.18 the laser efficiency behaviors vs. gas pressure are shown. Calculations were carried for different gas cell lengths (10 cm for fig. 1.17 and 40 cm for fig. 1.18) and different cavity losses (see plots legends). The curves for single – longitudinal - mode pumping (intra-cavity selector band-width 1 GHz) are shown by solid lines, and for multiple modes pumping (10 GHz selector) by dash lines.

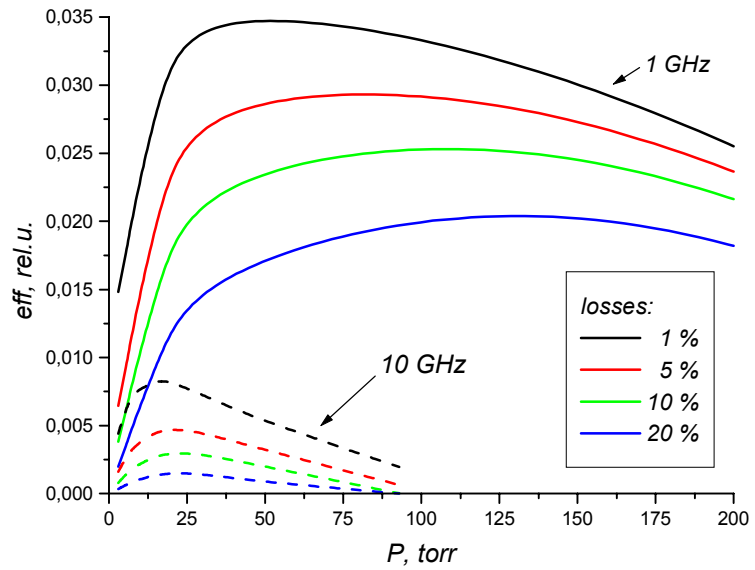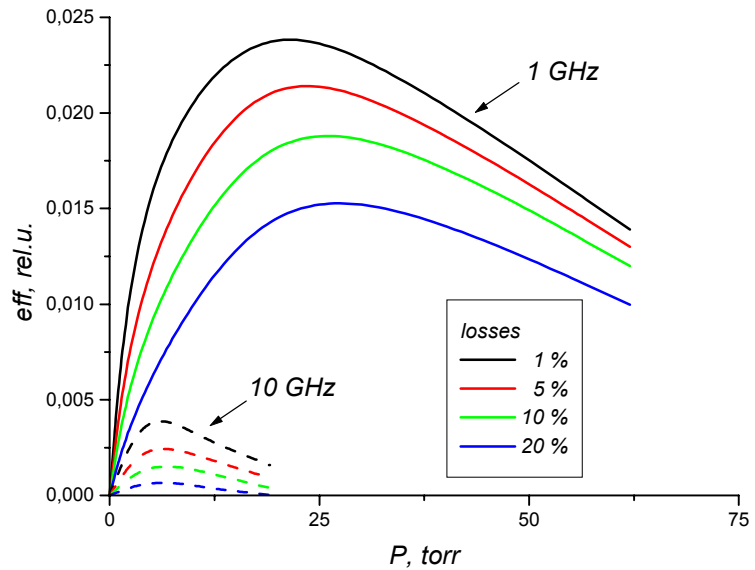Due to the V-V relaxation taken into consideration the curves have a maximums. The optimal

Fig. 1.17

Fig. 1.18

---

i   We have to mention, that for below simulations the V-V relaxation have been taken into account doubly. Firstly, as a short life-time of the upper laser levels ($\tau_G = 50$ nsec), secondly, by the eq. (9). Thus, the influence of the V-V relaxation was overestimated and we consider the simulation results are follows as a low limit.
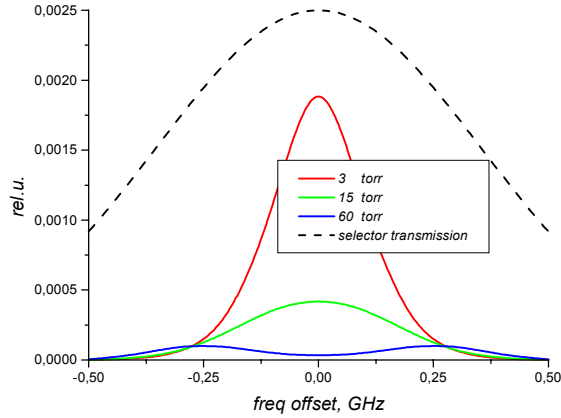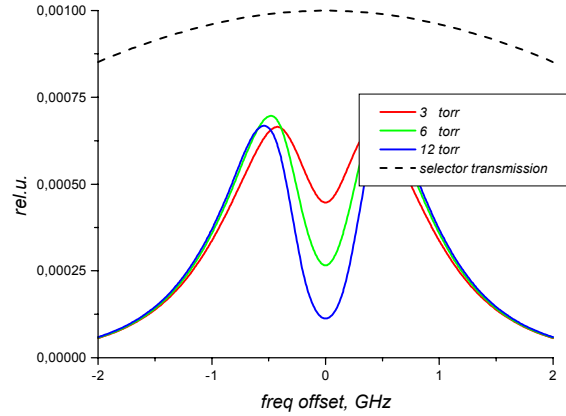
Fig. 1.19

Fig. 1.20

pressure depends not only on the cell length, but on the pump laser line-width and laser cavity losses at the pump wave-length too. This effect could be explained from the temporal behaviors of the molecular laser emission. The less selective or high-loss cavity makes the pumping less intensive and the molecular laser pulse longer. Therefore the V-V relaxation in the medium have more effect. Thus, for optimization of the gas cell parameters is important to take into account the laser cavity parameters.

At the fig. 1.19 and the fig. 1.20 are shown the spectral distributions of the pump laser emission for 40 cm gas cell length and different gas pressures. The left plot is corresponded to the narrow-band pumping (1 GHz selector) and the right plot corresponded to the multiple mode pumping (10 GHz selector). The green curves correspond to the optimal gas pressure (see fig. 1.18). One can see that in this case the depth of the hole in the spectral distribution of the pump laser emission is equal approximately 50 percent.
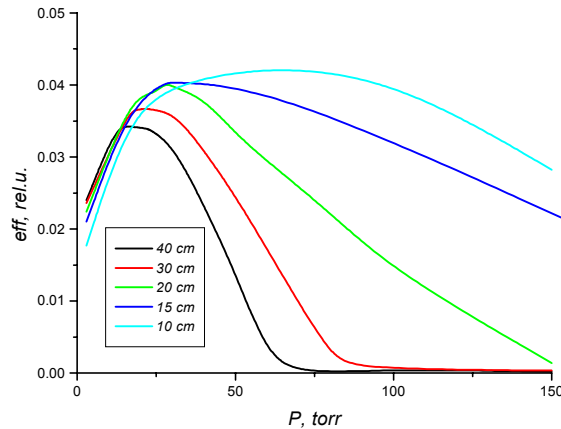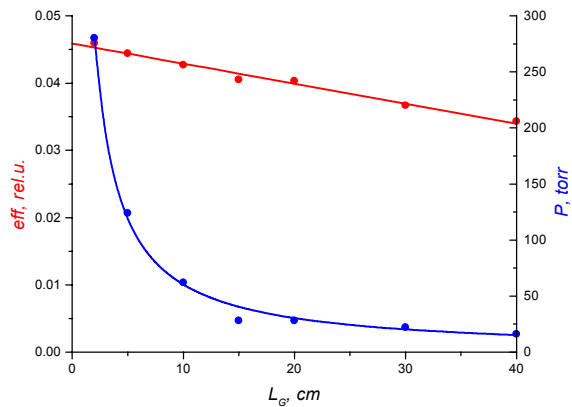

Fig. 1.21

Fig. 1.22

On the fig. 1.21 are shown the efficiency vs. pressure curves for different gas cell lengths and on the fig. 1.22 are shown the optimal pressure and maximum laser efficiency as a function of the cell length. This calculations were made for single-longitudinal-mode pumping and high Q-factor laser cavity. From the pictures follows that the use of a short cell is preferable for the molecular laser with intra-cavity pumping. Firstly, because of the higher output. Secondly, because of the low sensitivity to the pressure variations. As easy to see from the fig. 1.21, the peak corresponded to the short cell is not so sharp as a long cell peaks. However, for the very high pressure conditions, the model of molecular medium we use should be improved.

* * *

The conclusions of this section are following. The V-V relaxation processes in the molecular medium makes the mid-infrared laser output more sensitive to the spectral characteristics of the pump radiation and the pump laser cavity parameters. The use of multiple-longitudinal-mode pumping (10 GHz selector) instead of the single-longitudinal-mode pumping (1 GHz selector) causes approximately 5 times decrease of the laser output (for the high Q-factor cavity and the optimal gas pressure). For the broad-band pumping additional cavity loses at the pump wavelength cause the rapid fall of the molecular laser efficiency. However, for the narrow-line pumping, even high (10 – 20 %) round-trip losses decrease the laser efficiency for only about 30 – 50%.

Due to the V-V relaxation, the optimization of the gas cell parameters (relationship between cell length and gas pressure) became also more important. In contrast with external-cavity pumping, the use of the short gas cell looks preferable for the intra-cavity pumped molecular laser. The optimal gas pressure increases slow enough with the lengthen of the gas cell (20 torr for 40 cm cell, 50 torr for 10 cm cell). However, for the modeling of the short-cell high-pressure molecular lasers, the mathematical model of the molecular medium have to be improved.

1.3. The optical pumping of the molecular gas laser by GGG:Nd solid state laser

1.3.1. Introduction

The schematics of the molecular laser with GGG:Nd laser pumping are shown at the fig. 1.23. The laser system consist of the GGG:Nd laser head, the gas cell and the cavity optics. The lamp pumping of GGG:Nd and Q-switched cavity were considered. Three configurations of the laser system were modeled: the intra-cavity pumped molecular laser (fig. 1.23 part a), the extra-cavity pumped laser (fig. 1.23 part b) and the intra-cavity pumped laser with ring-cavity (fig. 1.23 part c).
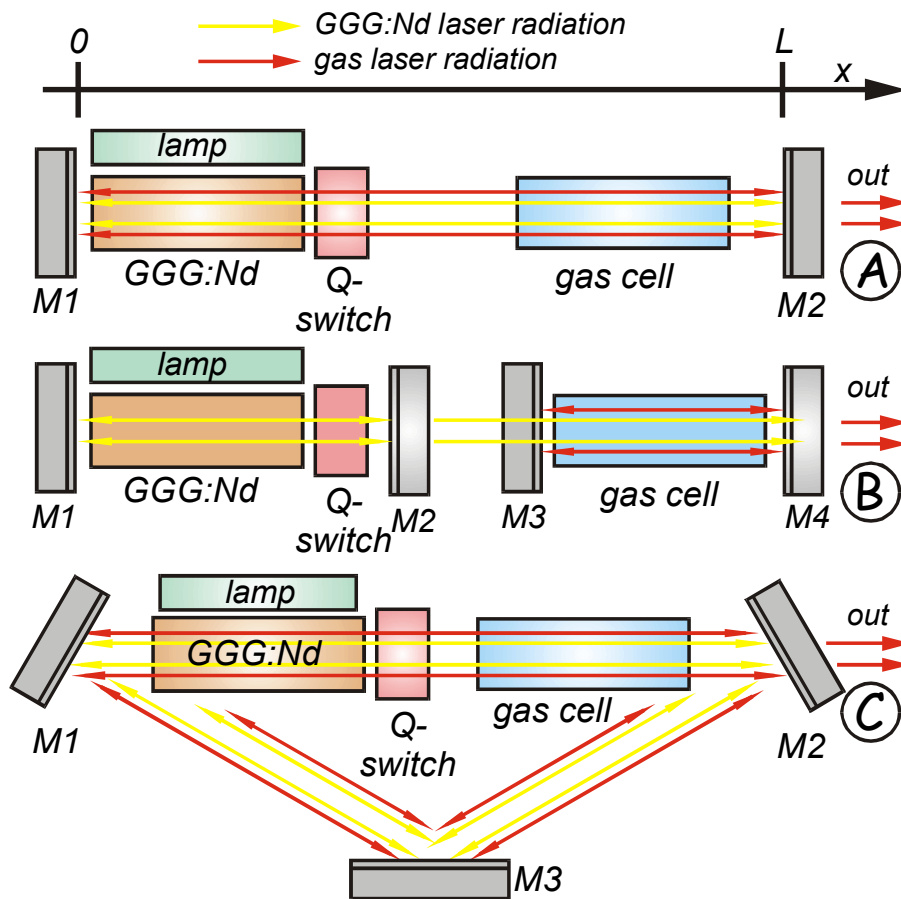

Fig. 1.23

The major parameters of the laser system are:

- Molecular pump (GGG:Nd laser)

    o *wavelength .... 1.33 μ*

    o *active crystal length .... 5 cm*

    o *GGG:Nd laser cavity transmission contour band-width 10 – 20 GHz*

- Molecular laser (HF laser)

    o *wavelength .... ≈3 μ*

    o *pump transition .... V0 → V2*

    o *gas cell length .... 10 - 40 cm*

    o *gas absorption line-width ..... 0.5 GHz*

The secondary parameters of the laser system are shown in the table below:

PARAMETER	*DESIGNATION*	*VALUE*	*UNITS*
active centers concentration in GGG:Nd crystal	N_C	$3{\times}10^{20}$	cm^{-3}
GGG:Nd crystal amplification factor	k	*0.36*	cm^{-1}
parasitic absorption in GGG:Nd crystal	η	*0.003*	cm^{-1}
effective cross-section of the stimulated emission (in the maximum of the luminescence contour)	σ_C	$1{\times}10^{-19}$	cm^{2}
characteristic time of spontaneous transitions in GGG:Nd crystal	τ_C	$2{\times}10^{-4}$	*sec*
gas molecules concentration	N_G	$5{\times}10^{16}$	cm^{-3}
absorption/emission effective cross-section of the gas medium at the pump wavelength	$\widetilde{\sigma}_G$	$1{\times}10^{-18}$	cm^{2}
absorption/emission effective cross-section of the gas medium at the purposeful wavelength	σ_G	$1{\times}10^{-15}$	cm^{2}

All the results presented in this section were obtained in approximation of the V-V relaxation-less gas medium.

1.3.2. *The laser cavity model*

Two types of the radiation are propagates the cavities: the GGG:Nd laser radiation and the molecular laser radiation. In contrast with the part. 1.3 of the report, the pumping into the second overtone was considered. Therefore, the eq. (7) were used as a rate equations for the gas medium.

The rate equation for GGG:Nd crystal have been written out in the section 1.2.3 of the report (see. eq. (11)). The transfer equations for the laser radiation are following:

- *GGG:Nd laser radiation:*

$$\begin{cases} \left(\dfrac{1}{c}\dfrac{\partial}{\partial t}+\dfrac{\partial}{\partial x}\right)f_C(\nu)=\sigma_C(\nu)N_C f_C(\nu)-\eta f_C(\nu) & x\in GGG:Nd \\ \left(\dfrac{1}{c}\dfrac{\partial}{\partial t}+\dfrac{\partial}{\partial x}\right)f_C(\nu)=-(N_{G0}-N_{G2})\tilde{\sigma}_G(\nu)f_C(\nu) & x\in gas\,cell \end{cases}$$

(1.21.)

- *the molecular laser radiation:*

$$\begin{cases} \left(\dfrac{1}{c}\dfrac{\partial}{\partial t}+\dfrac{\partial}{\partial x}\right)F_G=(N_{G2}-N'_{G0})\sigma_G F_G+\omega\dfrac{N_{G2}+N_{G1}}{\tau_G} & x\in gas\,cell \\ \left(\dfrac{1}{c}\dfrac{\partial}{\partial t}+\dfrac{\partial}{\partial x}\right)F_G=0 & x\notin gas\,cell \end{cases}$$

(1.22.)

there N_C is the inverse population at the GGG:Nd crystal laser transition; N_{Gi}, is the energy levels populations of the molecular medium [cm^{-3}]; η is the parasitic losses of the GGG:Nd crystal [cm^{-1}]; τ_G is the life-time of the upper laser level in the molecular medium [sec].

The rate equations (7) and (11), the transfer equations (21) and (22) is necessary to complete by the initial conditions and boundary conditions.

o *the initial conditions*

$$f_C(x,t=0)=0$$
$$F_G(x,t=0)=0$$
$$N_{G2}(t=0)=N_{G1}(t=0)=0$$
$$N(t=0)=N_0$$

(1.23.)

the boundary conditions are depend on the laser cavity scheme and were written out in the same way as the boundary conditions (18, 19) (see section 1.2.2).

The luminescence contour of the GGG:Nd crystal and the absorption line of the gas medium were approximated by the Gauss functions:

$$\sigma(\nu)=\sigma^{(0)}\,exp\left[-\left(\dfrac{\nu-\nu_{C0}}{\Delta\nu_C/2}\right)^2\right]$$

$$\tilde{\sigma}_G(\nu)=\sigma_G^{(0)}\,exp\left[-\left(\dfrac{\nu-\nu_{G0}}{\Delta\nu_G/2}\right)^2\right]$$

(1.24.)

there the $\sigma^{(0)}$ is a maximum cross-section of the GGG:Nd laser emission, the $\sigma_G^{(0)}$ is a maximum cross-section of the molecular absorption, $\Delta\nu_C$ and $\Delta\nu_G$ are the line-widths.

1.3.3. The modeling results

optimization of the gas cell pressure

Intra-cavity pumping (fig. 1.23a) At the fig. 1.24 are shown the behaviors of the GGG:Nd laser output pulse (curve 1) and molecular laser output pulse (curve 2) as a function of the gas molecules concentration N_G. The efficiency K of the optical pumping (curve 3) have been determined as a ratio of the molecular laser output energy to the maximum energy of the GGG:Nd laser without gas cell loading:

$$K = \frac{E_G}{E_{GGG:Nd}^{max}} \times 100\% \qquad (25.)$$

there $E_{GGG:Nd}^{max}$ is equal 3.2 J.

Fig. 1.24

From the fig. 1.24 follows that there is an optimal value of the gas concentration with the maximum molecular laser efficiency about 5%. At that condition, the GGG:Nd laser efficiency is minimal.

Fig. 1.25

The temporal behaviors of the GGG:Nd laser and the molecular laser outputs for the optimal gas concentration are shown at the fig. 1.25. The molecular emission pulse follows the pump pulse with the delay about 0.5 nsec.
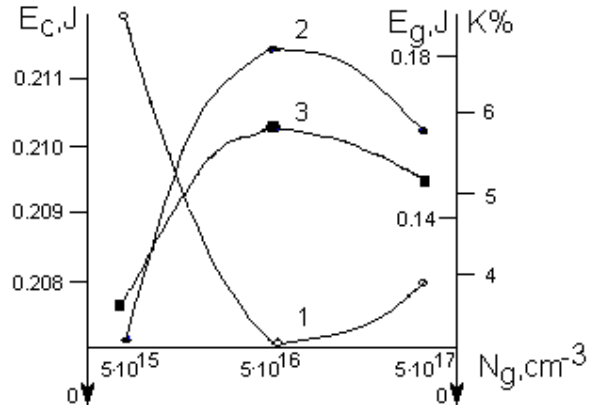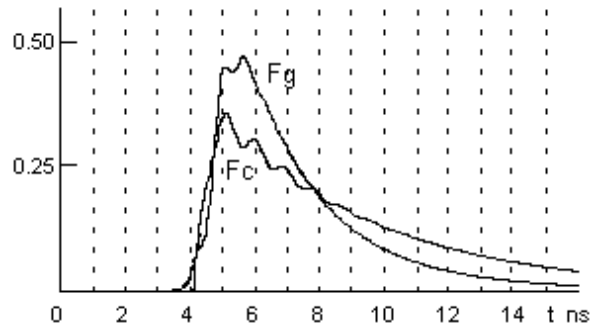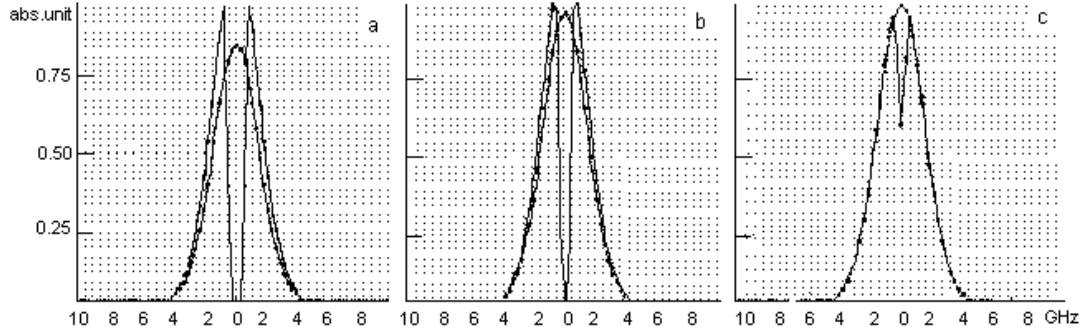
Fig. 1.26

The fig. 1.26 explains how the maximum of the K vs. N_G curve is apears. On the figure are shown the spectral distributions of the GGG:Nd laser emission. Part a of the figure coresponds to the high-concentration of the gas ($N_G = 5\times10^{17}$ cm^{-3}), part b corresponds to the optimal gas concentration ($N_G = 5\times10^{16}$ cm^{-3}), and part c to the lower-concentration of the gas ($N_G = 5\times10^{15}$ cm^{-3}). The spectral distributions of the GGG:Nd laser emission for zero gas concentration are shown by smoth contours.

If the gas concentration is too low (part c), then the pump laser spectrum is almost the same as the original GGG:Nd laser emission and only small hole apears in the spectral distribution. If the gas concentration is optimal (part b), then the hole in the spectral distribution reaches bottom. If the gas is over-concentrated (part a), then the pump laser emission at the gas absorbtion frequencies is almost suppresed and the lager part of the pump pulse energy is concentrated in the side-bands. As a result, the efficiensy of the optical pumping falls.

c) The intra-cavity pumping, ring laser cavity The behaviors of the pump laser output (curve 1), the molecular laser output (curve 2) and the molecular laser efficiency (curve 3) for the ring cavity configuration are shown at the fig. 1.27. Comparison of the fig. 1.27 and the fig. 1.24 shows, that the ring-cavity and the linear cavity schemes of the intra-cavity pumped molecular laser are quite similar. However, the linear cavity seems

Fig. 1.27

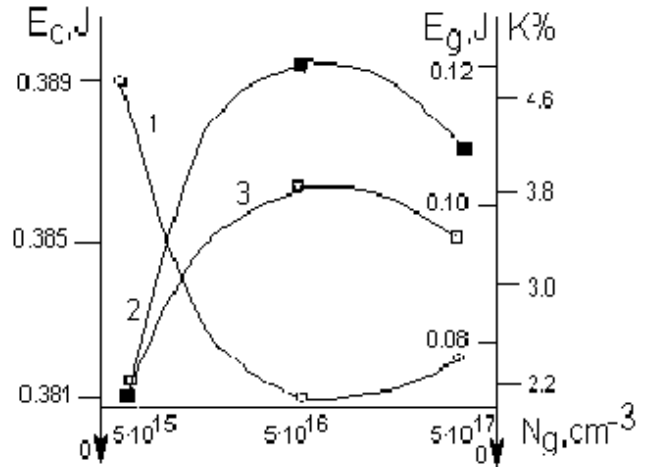preferable because of the higher efficiency (5.8% for the linear scheme and 3.8% for the ring scheme).

c) The external-cavity pumping At the fig. 1.28 are shown the behaviors of the pump laser output energy (curve 1), the molecular laser output energy (curve 2), and the optical pumping efficiency (curve 3) as a function of the gas concentration N_G. The cavity parameters were used for the modeling are shown at the fig. 1.29.
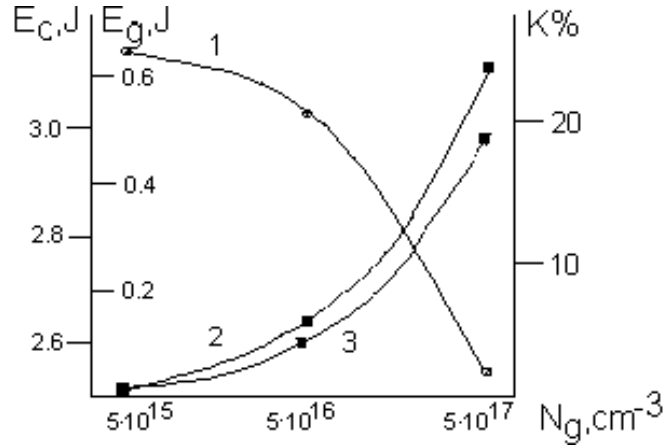

Fig. 1.28

In contrast with the intra-cavity pumping, the molecular laser output grows monotonously with increase of the gas concentration. The maximum efficiency of the molecular laser reaches 19% at the gas concentration about $N_G=5\times10^{17}$ см$^{-3}$. Such a difference between the intra-cavity and the external-cavity pumping schemes takes place because for the extra-cavity
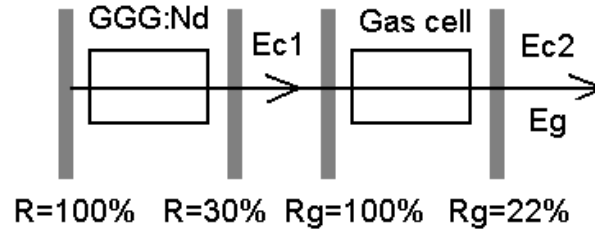

Fig. 1.29

pumping the gas cell absorption does not affect at the pump laser operation. However, for the low gas pressures the intra-cavity pumping scheme remains preferable (see the table below).

N_G, cm^{-3}	intra-cavity eff., %	extra-cavity eff., %
5×10^{15}	3.5	0.4
5×10^{16}	5.8	4.0
5×10^{17}	5.2	19

Optimization of the laser cavity parameters for intra-cavity pumping

The influence of the cavity mirrors characteristics and the parasitic losses in the GGG:Nd crystal at the molecular laser performance was studied. The optimal gas concentration $N_G = 5\times10^{16}$ см$^{-3}$ was used for the calculations. The GGG:Nd crystal non-saturated amplification factor was 0,358 см$^{-1}$.
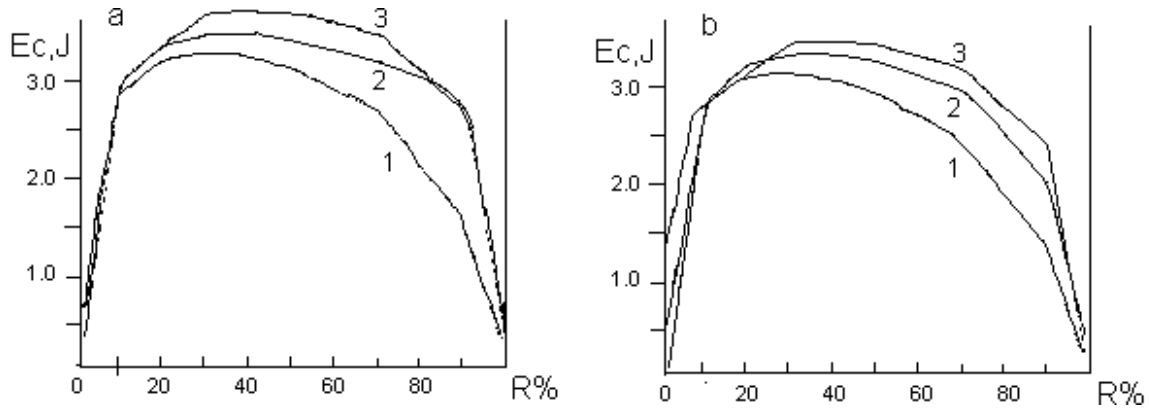
Fig. 1.31

At the fig. 1.30 are shown the GGG:Nd laser output energy as a function of the output mirror reflection at the GGG:Nd laser operation wave-length. The calculations were made for different levels of the parasitic losses in the GGG:Nd crystal: $\eta = 0.012$ cm^{-1} (curve 1); $\eta = 0.006$ cm^{-1} (curve 2); $\eta = 0.003$ cm^{-1} (curve 3). The part a of the figure corresponded to GGG:Nd laser without gas cell and part b corresponded to the laser with the gas cell (gas concentration $N_G = 5 \times 10^{16}$ см$^{-3}$).

Evidently, the GGG:Nd laser output increases with the decrease of the parasitic losses in the crystal. The optimal output mirror reflection also changes from 30% for $\eta = 0.012$ cm^{-1} to 40% for $\eta = 0.003$ cm^{-1}. The loading of the GGG:Nd laser cavity by the gas cell does not affect significantly at the curves shape and the maximums positions.

At the fig. 1.31 are shown the efficiency of the molecular laser K as a function of the cavity mirror reflection at the GGG:Nd laser operation wave-length (GGG:Nd laser cavity Q-factor). The calculations were carried out for the different levels of the parasitic losses in the GGG:Nd crystal (curve 1: $\eta = 0.012$ cm^{-1}; curve 2: $\eta = 0.006$ cm^{-1}; curve 3: $\eta = 0.003$ cm^{-1}). The important characteristic of the intra-cavity pumped molecular laser is the effective number of the pump beam passes through
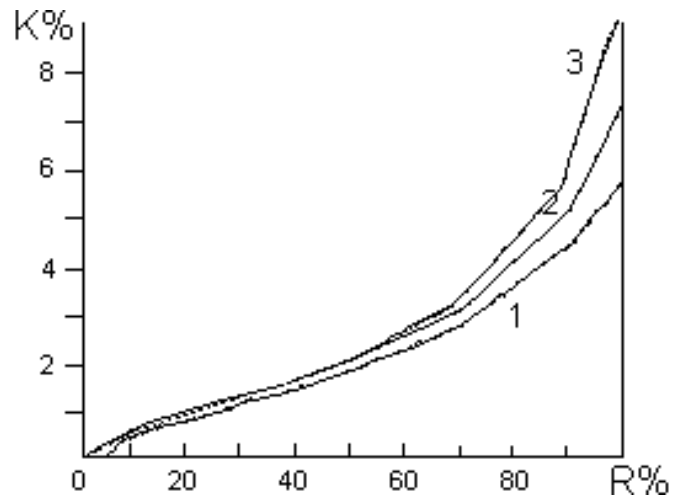

Fig. 1.30

the gas cell. Thus, the molecular laser efficiency grows rapidly with increase of the GGG:Nd laser cavity Q-factor. The level of the parasitic losses in GGG:Nd crystal became significant for the high-Q cavities (R > 80%).

Our calculations shows, that the GGG:Nd laser cavity Q-factor affects also at the spectral characteristics of the GGG:Nd laser emission. Half-width of the GGG:Nd laser spectrum increases from 3 GHz (R = 10%) up to the 4 GHz (R = 99%) due to the lower saturated gain. The parasitic losses in the GGG:Nd crystals have not any significant influence at the GGG:Nd laser spectrum.

Influence of the GGG:Nd laser spectral characteristics at the molecular laser performance

Parameters of the intra-cavity pumped molecular laser have been calculated. The two different band-widths of the GGG:Nd laser cavity transmission (Δv = 20 GHz and Δv = 10GHz) were considered. Other laser parameters were the same as in previous section. In the table below shown the calculated energy parameters of the laser system:

Δv,GHz	E_cJ	E_gJ	K, %
20	0.674	0.313	8.3
10	0.599	0.692	18.2

From the table follows, that the decrease of Δv from 20 to 10 GHz, causes the rise of the molecular laser efficiency by a factor 2.2.

The temporal profiles of the GGG:Nd laser (Fc) and the molecular laser (Fg) are shown at the fig. 1.32. With the decrease of the GGG:Nd fluorescence band-width Δv (Δv = 20 GHz for curve a) and Δv = 10 GHz for curve b) the peak power of the molecular emission increases. However, the molecular laser pulse duration remains constant. The
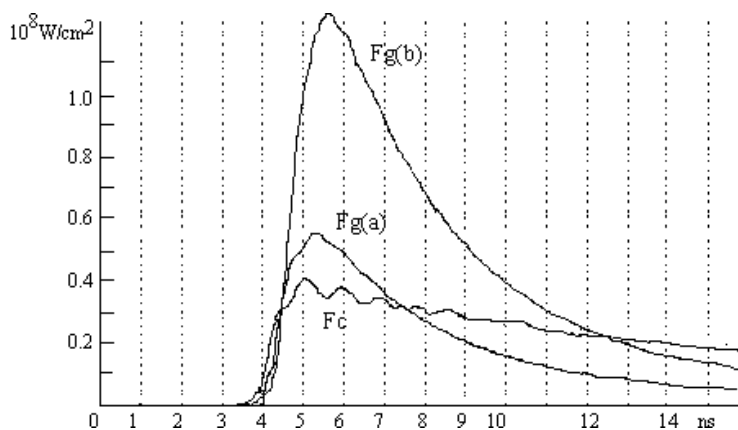

Fig. 1.32

temporal shape of the GGG:Nd laser pulse is almost the same for the both cases. The temporal dynamics of the gas medium energy levels population does not depend on $\Delta\nu$.

Temporal dynamics of the GGG:Nd laser emission

Temporal profiles of the GGG:Nd laser (Fc) and the molecular laser (Fg) pulses are shown at the fig. 1.33 and the integral spectrum of the GGG:Nd laser emission is shown at the fig. 1.34. The following series of the figures shows the temporal development of the GGG:Nd laser spectrum as the band-width of the GGG:Nd crystal fluorescence line was 20 GHz. The grid lines spacing on the figures is 0.5 GHz.
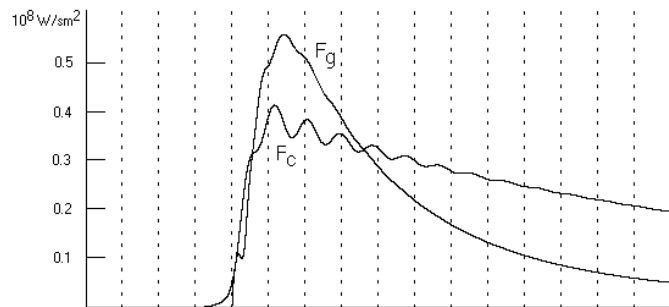

Fig. 1.33

fig. 1.35a The 0,1 ns after the Q-switch opening, the small narrowing appears in the GGG:Nd laser spectrum. At the same time in the spectrum appears a little hole due to the gas cell absorption.
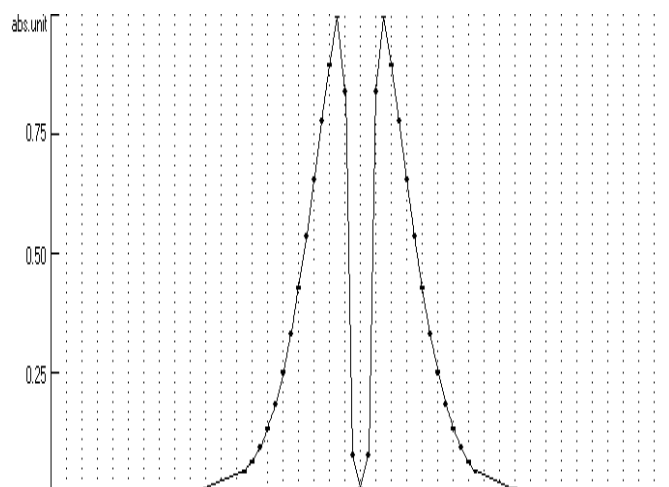
fig. 1.35b   After 1 nsec of the operation the GGG:Nd laser line-width decreases to 10 GHz (two times smaller than the band-width of the GGG:Nd laser cavity transmission).

Fig. 1.34

fig. 1.35c   At 5-th nanosecond the GGG:Nd laser line-width reaches 5 GHz and the gas absorption hole reaches the bottom of the spectral distribution.

fig. 1.35d-f   The GGG:Nd laser line-width does not changes till the end of the laser operation. The gas absorption hall expanding from the 0.5 GHz at 10 nsec to the 1 GHz at the end of the laser operation.
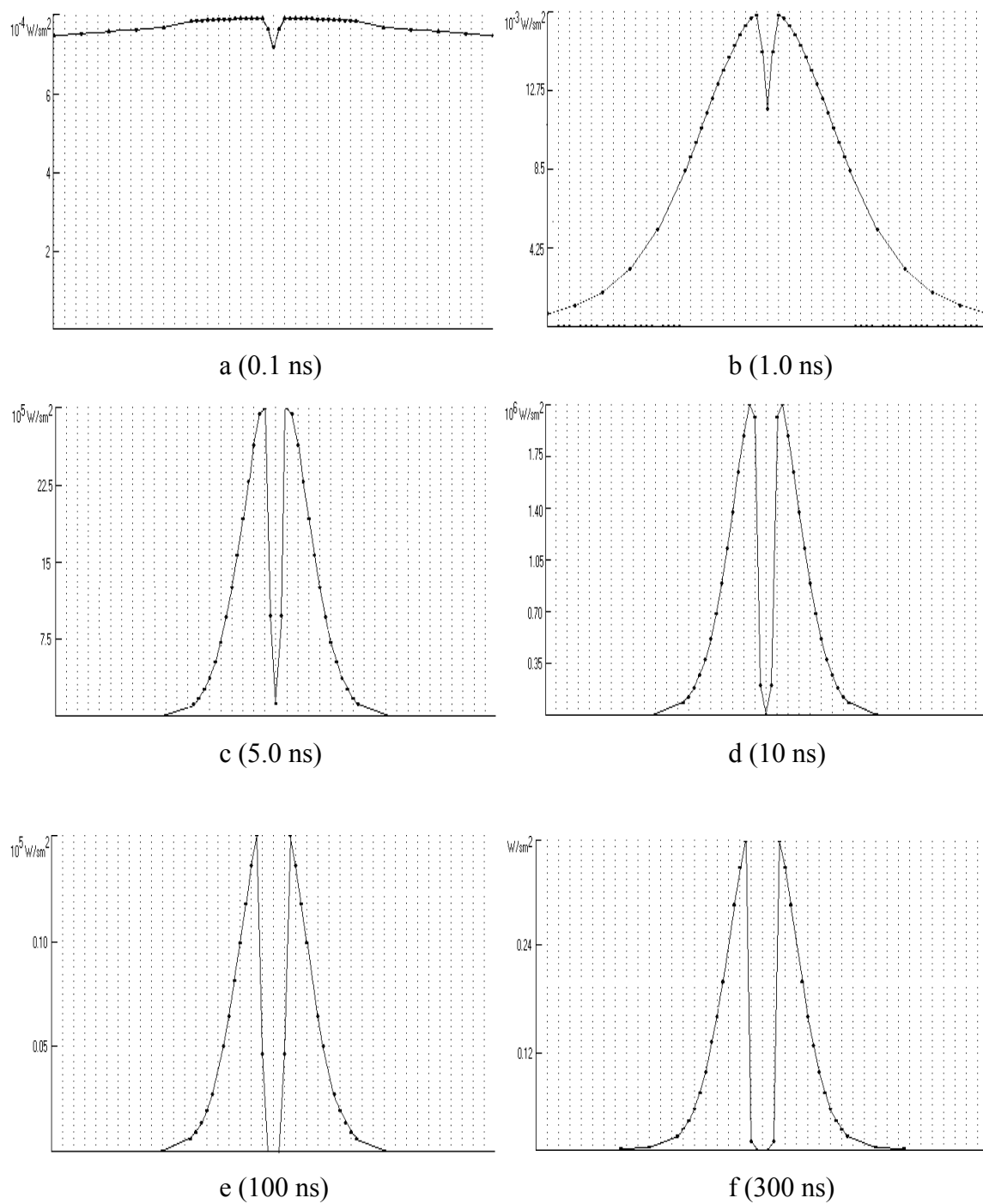
a (0.1 ns)

b (1.0 ns)

c (5.0 ns)

d (10 ns)

e (100 ns)

f (300 ns)

Fig. 1.35

Conclusions

In the report are presented the results of the theoretical study of the optically pumped molecular laser. The study was carried out by the computer simulation method. The particular features of the optically pumped molecular laser model are the simplified kinetic model of the gas medium and the multiple-spectral-components model for the pump laser radiation. Such an approach have allowed to simulate more rigorously the pump radiation narrowing in the dispersive laser cavity.

The study have included three parts: the development of the numerical model itself and development of the computer code; modeling and optimization of the molecular laser intra-cavity pumped by the $LiF : F_2^-$ color-center laser radiation; modeling and optimization of the molecular laser with GGG:Nd laser pumping. In the last case the intra-cavity and external-cavity pumping schemes were studied.

The study of the molecular laser with the intra-cavity optical pumping by the $LiF : F_2^-$ laser have included a several steps. Firstly, the numerical model was checked and the conditions of the model adequacy were determined. Then, the optimization of the gas cell parameters was carried as well as the simplified and more rigorous models of the V-V relaxation in the gas medium were compared. Finally, the basic requirements to the laser cavity parameters have been found.

The modeling of mid-IR laser with GGG:Nd laser pumping was carried out with simplified model of V-V relaxation in molecular medium. The different schemes of the optical pumping were compared (intra-cavity, ring-intra-cavity, external-cavity). The influence of the GGG:Nd laser radiation spectral parameters at the molecular laser performance was studied, and the spectral narrowing of the GGG:Nd laser emission in the dispersive cavity was investigated.

* * *

The main conclusions of the whole our study are following. The possibility of the effective molecular laser operation with intra-cavity and external-cavity optical pumping have been demonstrated. The intra-cavity optical pumping scheme looks preferable. Because, in contrast with the extra-cavity pumping, the shorter gas cell with lower pressure could be used.

Thus, the intra-cavity pumping scheme allows to realize more compact mid-infrared laser source with higher output quality.

The particular problem of the intra-cavity pumped molecular laser practical realization is a high requirements to the laser cavity. Firstly, the cavity should be high dispersive at the pump laser wave-length to provide the narrow-line pumping of the molecular medium (the cavity round-trip transmission band-width about 2 – 3 GHz). Secondly, the cavity Q-factor at the pump laser wave-length should be also high (round-trip losses less than 30%). The use of a standard laser optics does not allows to satisfy both abovementioned requirements. Thus, the development of a novel high-effective dispersive optical components is required.

The numerical model of the optically pumped molecular laser, we have developed, could be considered as an adequate for the qualitative study and optimization of the laser system. However, the further development of the mathematical model (the complication of the molecular medium model), is required to make more precise quantitative predictions.

2. High overtone molecular gas pumping experiments.

2.1. Tunable 1.3 μm neodymium laser for gas excitation

The aim of this part of work was to develop solid state laser for pumping gas media. The $(2 \leftarrow 0)$ obertone in HF has a multiple line structure in $1.25 \div 1.4$ μm spectral region. The frequencies of absorption on some vibration-rotation lines in HF $(2 \leftarrow 0)$ transition are close to $^4F_{3/2} \rightarrow {}^4I_{13/2}$ lasing transition of Nd^{3+} ions in garnet materials. It is well known that the lattice constants and crystal symmetry determine the value of Stark splitting and homogeneous broadening of energy levels of Nd^{3+} ions. We tried to find appropriate Nd doped crystalline medium which can provide high cross section value and exact wavelength to overlap with desired HF molecular gas absorption wavelength, and to test the possibility of its broader fine tuning.

Gadolinium garnet crystals were chosen as the most perspective media for HF excitation as their laser transitions are located very close to absorption lines. Fig. 2.1 presents the luminescence spectrum of $^4F_{3/2} \rightarrow {}^4I_{13/2}$ transition in Nd^{3+}:GGG crystal at room temperature and P(3), P(4), P(5) and P(6) absorption lines in HF $(2 \leftarrow 0)$. One can see that the most intensive fluorescence line of Nd^{3+}:GGG is centered at 1331.4 nm which is only slightly shifted from P(4) HF$(2 \leftarrow 0)$ absorption line (vacuum wavelength 1330.67 nm). Other rotational components of $\nu = 2 \leftarrow 0$ transitions absorption lines are located rather far from Stark-Stark transitions in Nd^{3+}:GGG expected to lase and can hardly be reached by use of this medium.

To investigate the oscillation of Nd^{3+}:GGG laser and its tunability we developed the experimental setup composed of the laser with power supply unit

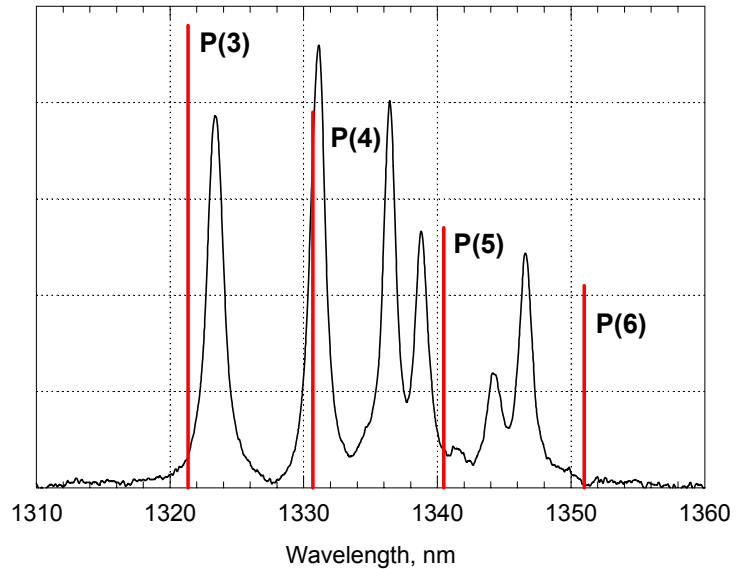*Fig. 2. 1 Fluorescence spectrum of $^4F_{3/2} \rightarrow {}^4I_{13/2}$ transition in Nd^{3+}:GGG crystal at room temperature and absorption lines in HF (2 ← 0).*

(Fig. 2.2). The temperature of the cooling liquid was controlled by the closed cycle refrigerator or heat exchanger. The output laser energy was measured by energymeter IMO-2H. To measure the precise wavelength value the laser oscillation was frequency doubled in $LiNbO_3$ crystal and measured by precise wavelength-meter developed in our Institute. The wavelength meter is based on four Fizo interferometers with increasing thickness. The accuracy of wavelength measurement depends on the laser linewidth and the number of interferometers in use. For laser linewidth $0.5 \div 0.05$ cm^{-1} three interferometers are in use that corresponds to the accuracy of $0.1 \div 0.02$ Å in the working region. For narrower linewidth, when all four interferometers operate the accuracy of wavelength meter is increased to $0.005 \div 0.002$ Å.

The stimulated emission cross section of $^4F_{3/2} \rightarrow {}^4I_{13/2}$ transition in neodymium laser crystals (~1.3 µm) is lower than that for $^4F_{3/2} \rightarrow {}^4I_{11/2}$ transition (~1.06 µm). So it is necessary to use optical elements in the cavity with antireflection coatings for 1.06 µm wavelength to prevent parasitic oscillations. The oscillation wavelength of the Nd^{3+}:GGG laser in the nonselective cavity with two mirrors was measured to be 1331.4 nm that corresponds to the maximum in the fluorescence spectrum. There are two possibilities to tune the oscillating wavelength. Firstly, we can use the cavity with dispersive element: either Fabri Perrot etalon, or diffraction grating. Secondly, we can change lattice constant, Stark splitting and frequency of Stark-Stark transitions by cooling or heating the laser active element.
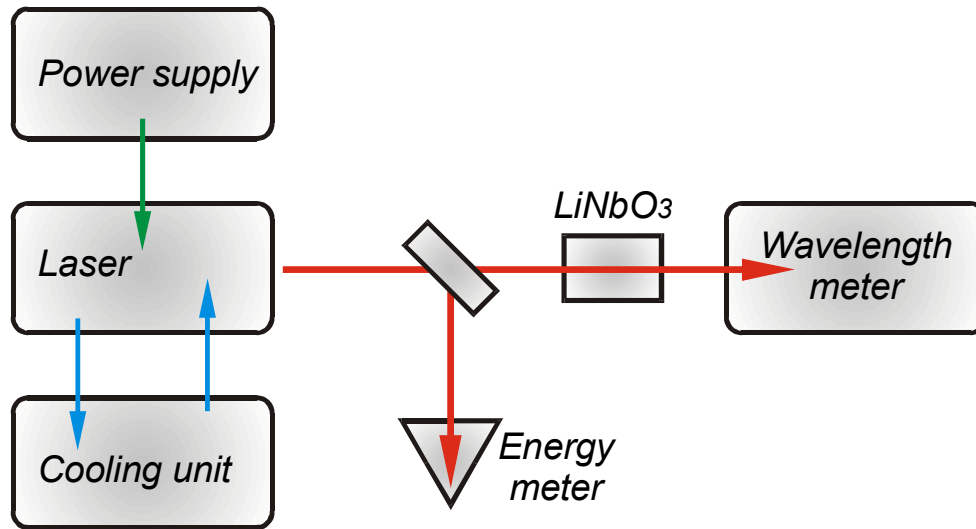

Fig. 2. 2 Experimental setup for measuring spectral and energy characteristics of neodymium lasers.

Fig. 2.3 presents three optical schemes of Nd^{3+}:GGG laser cavities. The active crystal was placed into the Ce-doped chamber with a pulsed flash lamp. The chamber was either cooled or heated by water from the temperature controlled thermostat unit. The first nonselective scheme (Fig. 2.3,a) was composed with HR mirror with R=3m curvature (M_1). The flat output coupler (M_2) has R=38% reflectivity at 1.3 μm wavelength. For Q-switching we used quarts based acoustooptic cell guided by high frequency generator. With 75 J pump energy to the flash lamps the laser provided oscillation pulses of 220 mJ at 3 Hz pulse repetition rate.

The temperature dependence of wavelength tuning with Nd^{3+}:GGG active element heating is shown in Fig. 2.4. Heating the crystal till 80°C temperature results in 4Å increase of the oscillating wavelength. In the linear approximation to reach the required HF wavelength one needs to cool active element to -70°C degrees. This requires to use special cooling thermostat and liquids to protect system freezing and vacuumed cryogenic optical cavity which strongly increase system complexity.
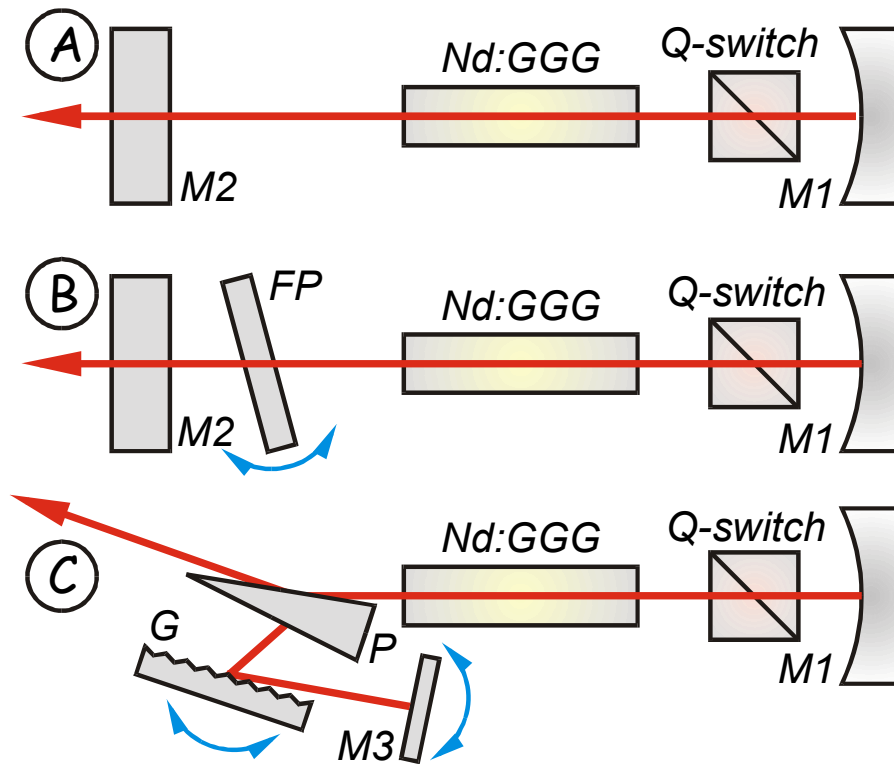

Fig. 2. 3 Optical scheme of laser cavity for testing neodimium laser operation in nonselective (A) and dispersive (B, C) schemes. Scheme includes Fabri Perrot etalon (FP) and prism telescope (P) and diffraction grating (D) as dispersive elements.

Dispersive scheme (Fig. 2.3,b) includes glass Fabri Perrot etalon with 1 mm thickness and 55% reflectivity mirrors. By changing the incident angle we were able to tune the laser wavelength inside etalon order. The tuning curve of Nd^{3+}:GGG laser with Fabri Perrot etalon is shown in Fig. 2.5. The tuning range spread from 1331.06 to 1331.29 nm. The further tuning of Fabri Perrot etalon resulted in the

Fig. 2. 4 Temperature tuning of Nd^{3+}:GGG laser wavelength in nonselective cavity.

oscillation jump to another Stark-Stark component of Nd^{3+}:GGG spectrum at 1336.4 nm. As a dispersive element Fabri Perrot has two drawbacks. It introduces high intracavity losses into the cavity due to high reflectivity at the mirror surfaces resulting in the lowering of the laser efficiency. Secondly there can be the competition between the wavelengths working in different interference orders. To overcome the last problem one needs to use additional etalons with different thickness.

Another dispersive scheme (Fig. 2.3,c) used prism telescope and diffraction grating. Single prism telescope was used to expand the beam in front of the grating to protect it from optical damage. It also worked as an output coupler of this laser. Rotating the prism we were able to control the output coupler efficiency and the expanding coefficient. Diffraction grating (1200 lines per mm) worked in the autocollimation scheme so
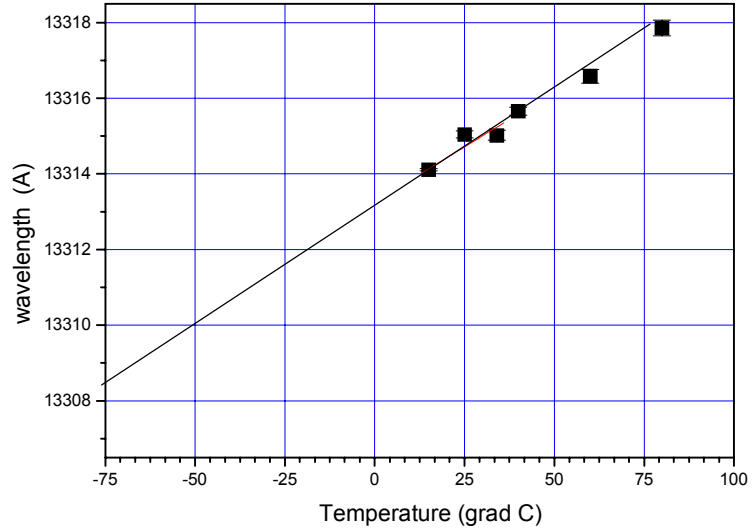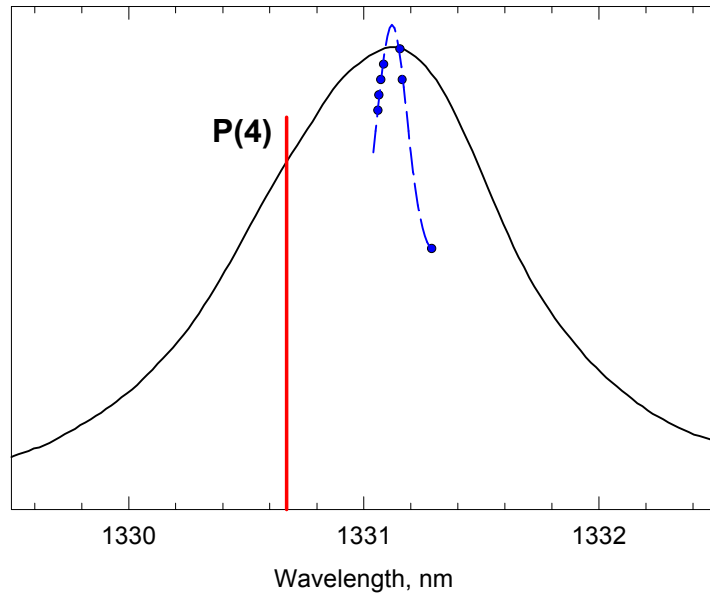

Fig. 2. 5 Fluorescence line of Nd^{3+}:GGG crystal and tuning of the oscillation wavelength of Nd^{3+}:GGG laser. The vertical line is the absorption line in HF(2←0) transition P(4) line.

that the first diffraction order (R~70%) was reflected back into the cavity. For some experiments below we used additional mirror M_3 to reflect zero order back into the cavity. The tuning curve of Nd^{3+}:GGG laser for two incidence angles of the prism is shown in Fig. 2.6. The filled triangles correspond to 81.5° grazing incidence angle. The tuning from 1330.8 nm to 1331.8 nm was observed with the output energy in the maximum of

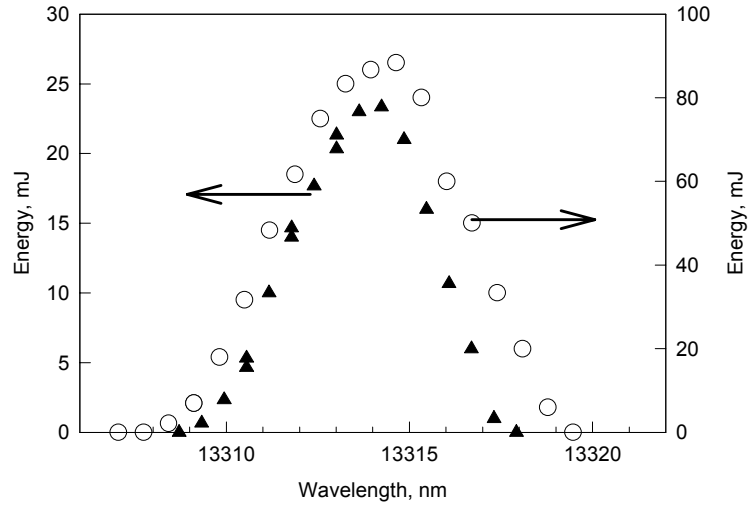*Fig. 2. 6 Tuning of Nd^{3+}:GGG laser in dispersive cavity with diffraction grating for grazing incidence angles 81.5° (filled triangles) and 79° (hollow circles).*

23 mJ. The output energy of 90 mJ and tuning range 1330.7 ÷ 13319.5 nm were observed when the grazing incident angle was reduced to 79°. The oscillation of Nd^{3+}:GGG laser didn't allow us to reached the required wavelength to overlap with HF(2 ← 0), P(4) line with good laser efficiency.

It is well known that Nd^{3+} luminescence bands depend on the type of the crystal and type of consisted cations. Fig. 2.7 presents fluorescence spectra of Nd^{3+} in different gadolinium garnets: GSGG, YSGG and YGG, which were poorly investigated in this spectral region in literature. Comparison of GSGG and YSGG crystals shows that in both crystals the $^4F_{3/2} \rightarrow {}^4I_{13/2}$ transition line around 1330.5 nm is split into two lines. The HF (2 ← 0) absorption

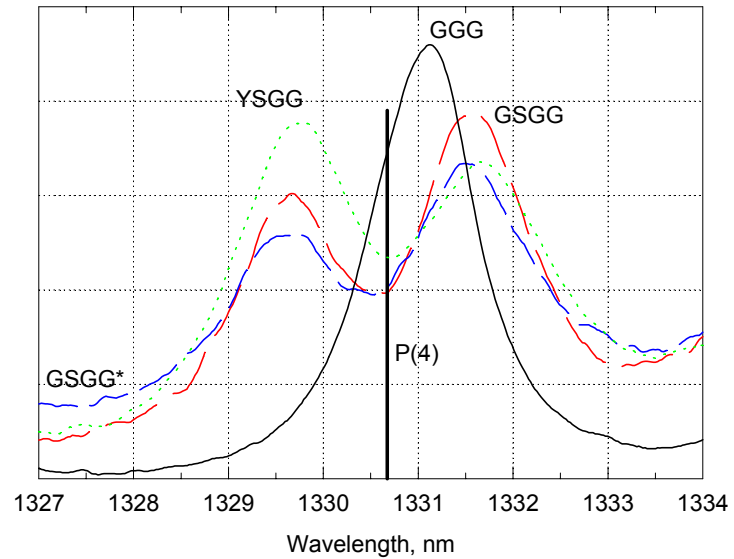*Fig. 2. 7 Fluorescence spectrum of $^4F_{3/2} \rightarrow {}^4I_{13/2}$ transition in Nd^{3+}:GGG, Nd^{3+}:GSGG and Nd^{3+}:YSGG crystals at room temperature and absorption line of HF(2 ← 0) transition P(4).*

line P(4) is located in between these two Stark-Stark transitions. In GSGG the line with longer wavelength has higher intensity and it can hardly be used for HF excitation. The YSGG crystal has similar Stark level structure but more intensive line is located in the shorter wavelength region.

For laser experiments we used Nd^{3+}:YSGG laser rod $\varnothing 6x100$ mm co-doped with Cr^{3+} for

Fig. 2. 8 Temperature tuning of Nd^{3+}:YSGG laser wavelength in nonselective cavity.

sensibilisation. The concentration of dopants in YSGG sample was $1\cdot10^{20}$ cm^{-3} for Cr and $3\cdot10^{20}$ cm^{-3} for Nd.

The oscillation of Nd^{3+}:YSGG laser in nonselective cavity proved our proposal to obtain oscillation at shorter wavelength. It provided us 1329.7 nm wavelength that corresponded to the maximum in the fluorescence spectrum. By heating the active element temperature we were able to shift the oscillation wavelength to longer wavelength. Fig. 2.8 presents our results on the temperature tuning of Nd^{3+}:YSGG laser wavelength. By heating of the heat exchanger liquid to 90°C we were able to shift the oscillation wavelength with 5Å to 1330.2 nm value. That was shifted to as close as 4Å from the absorption line P(4) in HF (2 $\leftarrow$ 0) transition we needed. From Fig. 2.9 follows that further heating to 120°C could give the required wavelength. At the same time at temperatures above 75°C we observed that the oscillation of Nd^{3+}:YSGG laser split into two lines at 1330 nm and 1332 nm that corresponded to two different Stark-Stark transitions. For higher temperature the laser wavelength was mostly 1332 nm. So the increase of the temperature results in the thermal redistribution between these lines.

The oscillation of Nd^{3+}:YSGG laser was investigated in the dispersive cavity (Fig. 2.3, c) to get the P(4) absorption line in HF (2 $\leftarrow$ 0) transition. Fig. 2.9 summarizes our results on laser oscillation in dispersive cavity. Open squares show data for Nd^{3+}:YSGG laser without mirror M3 at room temperature. One can see that the tuning range of the laser covered spectral region from 1329.4 nm to 1330.3 nm. Limited output energy was due to high cavity losses in the zero
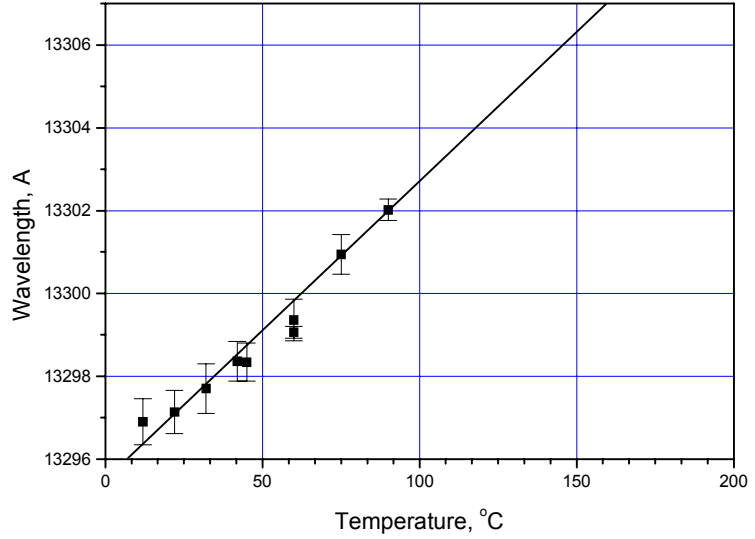
diffraction order of the grating. These losses also narrow tuning spectral range of the laser. To improve this scheme we installed HR mirror M3 to reflect zero order reflection back into the cavity. In this case tuning of oscillation wavelength required simultaneous rotation of diffraction grating and mirror M3. The output and intracavity radiation considerably increased so that this intensity could damage optical elements. Filled squares present results on the

Fig. 2. 9 Tuning curves of Nd³⁺:YSGG (squares and crosses) and Nd³⁺:GGG (hollow circles) lasers at room (crosses, circles and filled squares) and hollow squares at 65°C in dispersive cavities. Crosses and circles are without mirror M₃. Squares are with mirror M₃.

oscillation of Nd³⁺:YSGG laser with mirror M3 at room temperature. We observed tunable oscillation at two Stark components from 1329.1 nm to 1330.5 nm and from 1331.1 nm to 1332.3 nm. The absence of data points in the central part of the tuning curve (1330÷1331 nm) is due to very high energy that can destroy optical elements. By heating the crystal temperature to 65°C we were able to shift the longer wavelength edge to 1330.6 nm (Open squares in Fig. 2.9). This value is very close and only 0.5Å from the desired absorption wavelength in HF (2 ← 0), P(4), see bar in Fig. 2.9.

Thus from our fluorescence and laser experiments we found that well developed and available Nd³⁺:GGG, Nd³⁺:GSGG and Nd³⁺:YSGG laser crystals provide laser oscillation very close to absorption line of HF(2 ← 0) transition, but still there is no overlapping. Analysis of crystal lattice parameters allows us to predict the shorter wavelength shift of the central line in $^4F_{3/2} \rightarrow {}^4I_{13/2}$ transition in yttrium gadolinium garnet (Nd:YGG) in comparison with gadolinium gallium garnet (Nd:GGG). But this crystal is not available in the market and need more time and special order for growing. We synthesized a small spectroscopic sample to prove our prediction. Fig. 2.10 presents Nd³⁺:YGG fluorescence spectra. One can see that it has very good overlapping with desired wavelength. The linewidth is slightly broader than in Nd³⁺:GGG crystal that provides better possibilities of fine tuning the oscillating wavelength. In Nd³⁺:GGG laser the

tuning region was restricted by the highly intense neighbor line at 1337 nm so that the oscillating wavelength jumped to it. Lower intensity of this line in Nd^{3+}:YGG crystal allows to use laser cavity with higher selective losses without any jumps to another Stark-Stark transitions. The further work on growing, treatment and testing Nd^{3+}:YGG laser active elements with high optical quality can be evaluated in the future. And allows us to propose the successive solution for HF $(2{\leftarrow}0)$ molecular gas pumping by crystalline Nd laser.

Fig. 2. 10 Fluorescence spectrum of $^4F_{3/2} \to {}^4I_{13/2}$ transition in Nd^{3+}:GGG (dashed line) and Nd^{3+}:YGG (solid line) crystals at room temperature and P(4) absorption line of HF(2 $\leftarrow$ 0) transition.

2.2. Tunable LiF:F_2^- color center laser for gas excitation

In this work we developed LiF:F_2^- color center (CC) laser for pumping molecular gas media. Fig. 2.11 presents the tuning curve of LiF:F_2^- CC laser and absorption lines of HF $(2 \leftarrow 0)$ and HCl $(3 \leftarrow 0)$ transitions. One can see that tunable radiation overlaps with R and P branches of HCl $(3 \leftarrow 0)$ transition and with R-lines from HF $(2 \leftarrow 0)$ transition. The aim of our

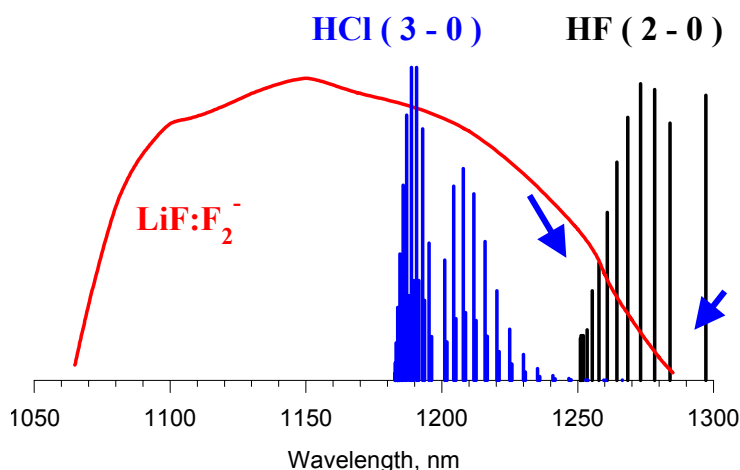*Fig. 2. 11 Tuning curve of LiF:F_2^- color center laser and absorption lines of HF($2 \leftarrow 0$) and HCl ($3 \leftarrow 0$) transitions.*

research was to develop powerful narrowline single frequency tunable LiF:F_2^- laser. The principal scheme of the laser is shown in Fig. 2.12. The laser was based on Nd^{3+}:$YLiF_4$ pump laser with single pass amplifier stage that produced up to 150 mJ with 30 ns pulse duration at 1.047 μm.

The pump beam was split into two beams which separately pumped LiF:F_2^- CC oscillator and amplifier. The pump beam excites the oscillator gain media with the help of 45-degrees intracavity dichroic mirror. This protects dispersive elements from optical damage. Mirror with 25-27% reflectivity in 1080-1270 nm spectral region was used as an output coupler.

Smooth tuning of LiF:F_2^- CC laser was one of our important tasks. For this purpose we measured tuning of the oscillating wavelength of our laser system with wavelength meter. Fig. 2.13 presents the oscillating wavelength with respect to the number of the stepping motor driver steps of. In this case we used only one dispersive element – diffraction grating.
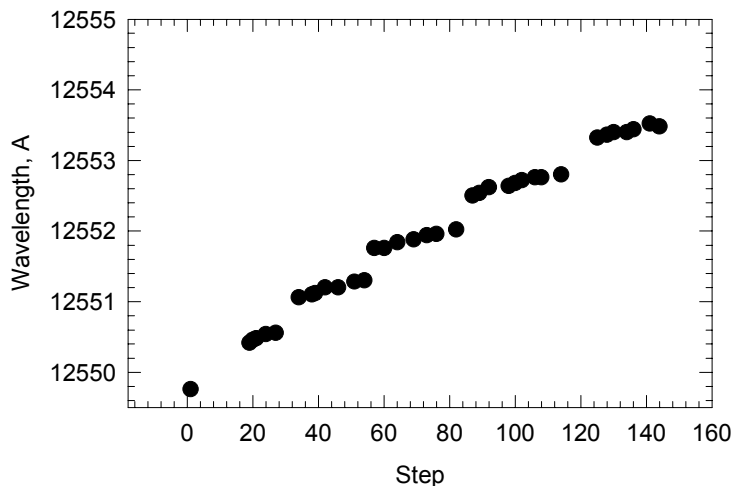
Fig. 2. 12 . Tunable LiF:F_2^- color center laser with power amplifier pumped by Nd^{3+}:$YLiF_4$ laser.

Fig. 2. 13 Tuning of LiF:F$_2^-$ color center laser wavelength via stepping motor driver steps. The instability is due to interference at the output coupler parallel surfaces.

One can see wavelength jumps in Fig. 2.13 that are due to interference and wavelength selective reflection on the output mirror with parallel surfaces. To remove this we used dichroic output coupler with wedge glass substrate. Fig. 2.14 shows smooth scanning of LiF:F$_2^-$ color center laser wavelength with stepping motor driver steps. This system allows us to search for gas absorption lines more precisely. The absorption transition on R-lines of HF (2 ← 0) could have higher cross section than HCl (3 ← 0) transition. So we decided to check absorption in HF cell first.
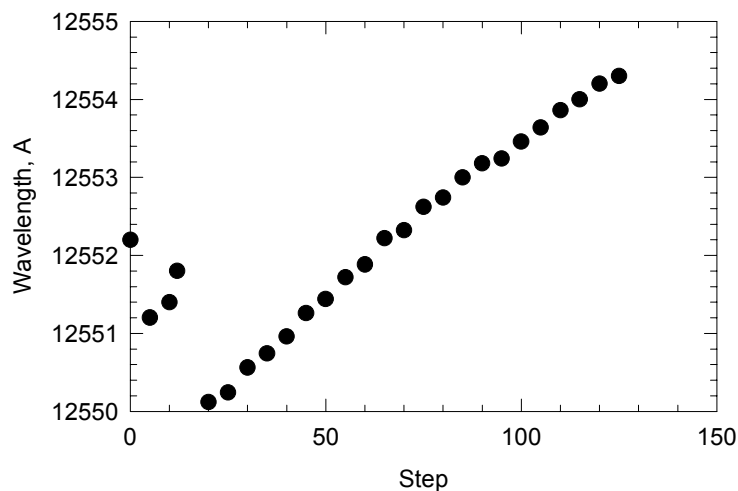

Fig. 2. 14 Tuning of LiF:F$_2^-$ color center laser wavelength via stepping motor driver steps with wedge mirror as an output coupler.
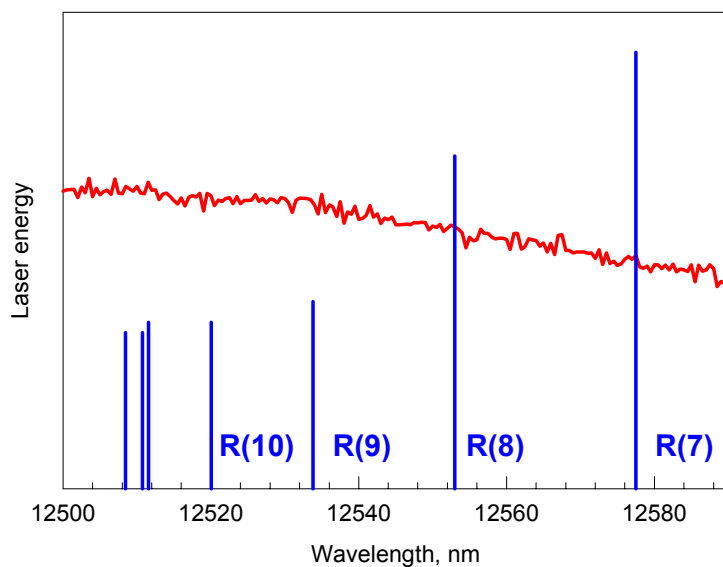
*Fig. 2. 15 Tuning of LiF:F$_2^-$ color center laser without gas cell and positions
of HF(2←0) absorption lines.*

One can see that the tuning region of our laser system allows us to excite R(7) – R(10) lines of HF(2←0) transition (Fig. 2.15). The improvement of laser cavity with intracavity Fabri Perrot etalon allowed us to observe absorption in the R(8) line of HF (2←0) transition (Fig. 2.16). The further improvement of our laser system will allow us to observe strong absorption and luminescence from gas to arrange conditions for solid state laser pumping of gas medium.
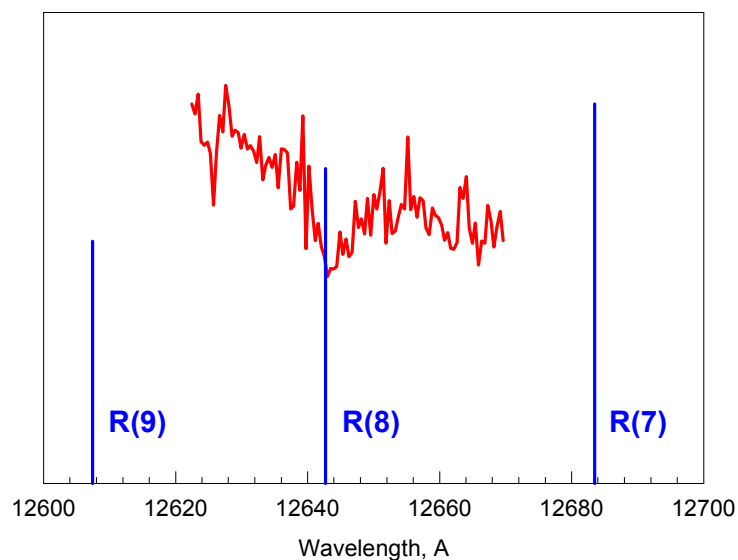

*Fig. 2. 16 Absorption of tunable radiation of LiF:F$_2^-$ color center laser by
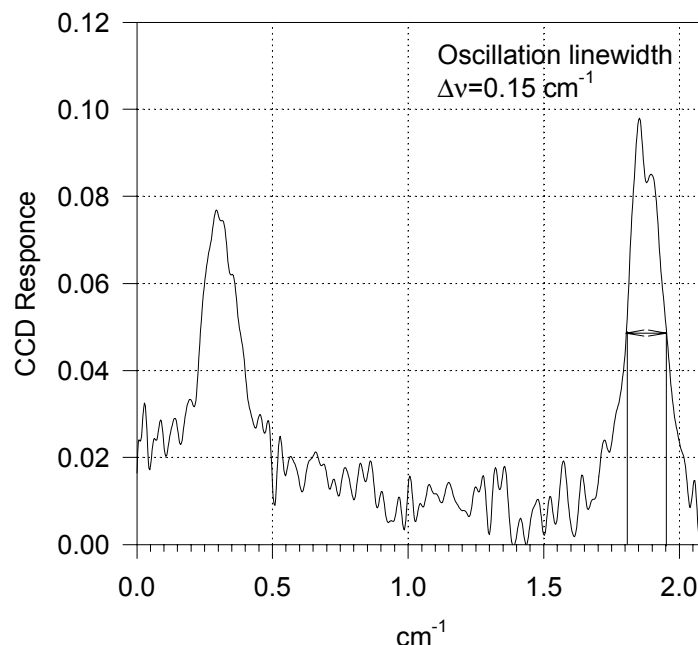R(8) line from HF(2←0) transition.*

Fig. 2. 17 Oscillation linewidth of the tunable narrowline LiF:F_2^- color center

laser

For further molecular gas fluorescence and oscillation measurements the scheme of the excitation LiF:F_2^- color center laser was modified to obtain sufficiently narrower oscillation linewidth. The optical scheme of the color center laser was designed to allow inserting of additional spectra selective elements inside the cavity. To obtain narrower linewidth 4x prism telescope together with intracavity etalon were mounted. The snapshot of the output laser spectra measured by Fizo interferometer and CCD linear array is shown in Fig. 2.17. The measured linewidth of the oscillation spectra was determined to less than 0.15 cm^{-1}. Though some problems existed concerning precise smooth simultaneous scanning of both spectral selective elements: grating and etalon. The angular position of each element is precisely computer controlled and can be easily set separately. All the necessary software modification to solve the problem were developed.

3.   The influence of various selective elements on the Narrow-line operation of LiF:F$_2^-$ color center tunable laser for molecular gas pumping.

Introduction.

To study the influence of various selective elements on the narrowline operation of LiF:F$_2^-$ color center laser the different schemes were developed and investigated. The scheme of the optical cavity with the grating placed at the autocollimation angle was selected as most simple and easy designed. As an alternative the scheme with the grating placed at grazing angle was also studied.

3.1. Optical scheme of the tunable color center pump laser.

The advantage of the scheme with the grating placed at grazing angle is sufficiently narrower linewidth due to larger dispersion. To combine this advantage with the simplicity of the autocollimation scheme the special grating was ordered and purchased. This gold grating has 830 grooves/mm and its working angle within 1.19-1.2 μm
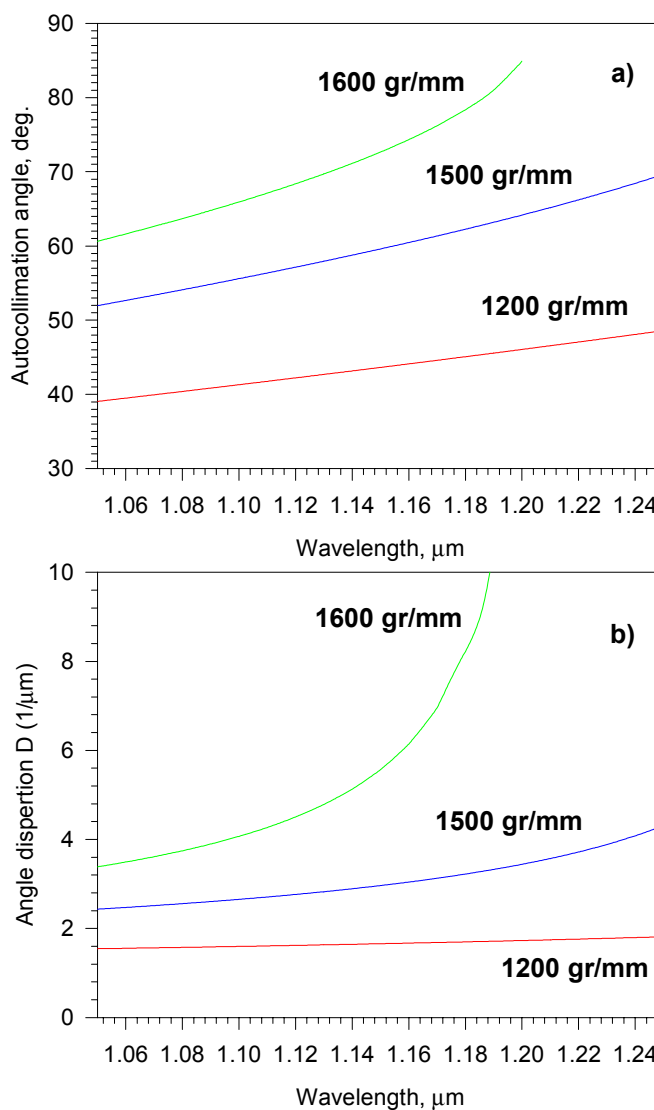

fig. 3. 1 Autocollimation angle versus wavelength (a) and angle dispersion D (b) for gratings with 1600, 1500 and 1200 grooves/mm.

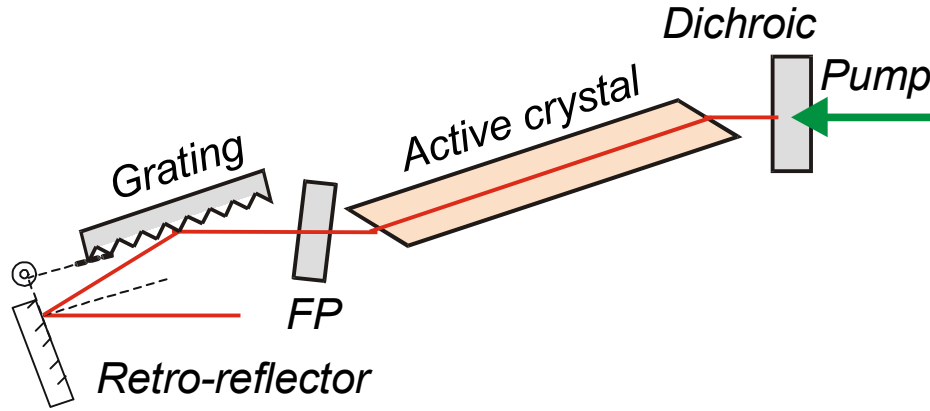*fig. 3. 2 Optical scheme of the narrowline tunable LiF:F$_2^-$ color center laser*

operating range is close to 80°, which is not far from the optimal 85° incidence angle for the grazing scheme (see Fig. 3.1(a)). As can be seen from the Fig 2.1(b) the grating with 1600 grooves/mm has sufficiently higher angular dispersion D within 1.19-1.2 μm range as compared to diffraction gratings with 1500 and 1200 grooves/mm. The 830 grooves/mm grating (25x25 mm size) is working in the second diffraction order so the output into the first diffraction order should be regarded as losses and thus minimized. For purchased grating the reflection into the second diffraction order was measured to be about 35% while reflection into the first diffraction order was less than 5% (for working horizontal polarization). The optical scheme of the laser using this grating is shown in Fig. 3.2.

The LiF:F$_2^-$ color center laser was pumped by the passively Q-switched YLF:Nd laser operating at 1.047 μm. The output energy of the pump laser was about 35 mJ and was horizontally polarized to match the required polarization of the color center laser. The total efficiency of LiF:F$_2^-$ color center laser was measured to be about 10%.The resulting tuning curve of the laser within 1.19-1.2 μm
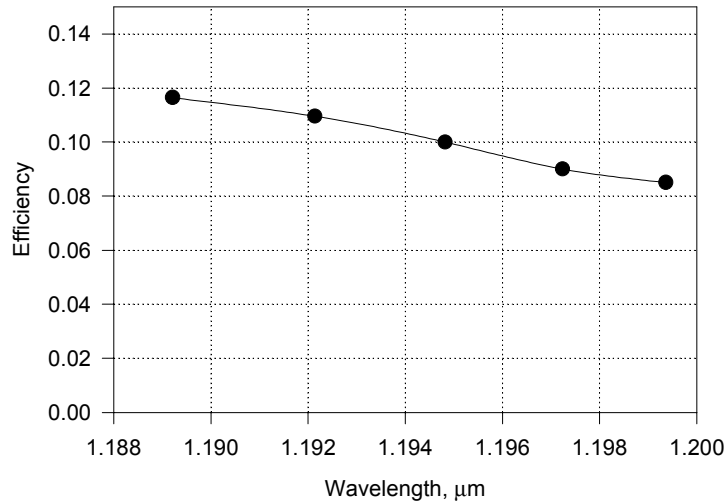

fig. 3. 3 Tuning curve of the LiF:F$_2^-$ color center laser within 1.19-1.20 μm wavelength range.

wavelength range near HCl (3←0) molecular gas absorption is shown in Fig. 3.3.

The linewidth of the laser was measured using the "Burleigh" Fabry-Perot interferometer. Due to large incidence angle the illuminated aperture of the grating was about 15 mm, thus increasing the selectivity of the traditional scheme. Without any additional selective elements inside the cavity the linewidth of the laser was measured to be 0.3 cm^{-1}.

fig. 3. 4 Calibration of the CC laser output wavelength using LRL005 computer controlled λ-meter.

To obtain narrower linewidth additional spectral selective elements should be added to the optical scheme. Most commonly used intracavity elements are beam expanders and Fabry-Perot etalons. Due to the limited aperture of the used grating the placement of intracavity telescope was practically senseless as practically all grating was illuminated even without any type of beam expander. Several Fabry-Perot etalons of different shape and transmittance were tested to evaluate their influence on the resulting linewidth. The results of the test are summarized in Table 2.1.

Type of Fabri-Perrot etalon	CC laser output energy, mJ	CC laser total efficiency	CC laser linewidth, cm^{-1}
60% REFLECTIVITY, 10 MM THICKNESS	1.2	3.4 %	0.1
85% reflectivity, 3 mm thickness	0.6	1.7 %	0.09
92% reflectivity, 3 mm thickness	0.4	1.1 %	0.08

Table 3.1. Output energy, efficiency and linewidth of the LiF:F$_2^-$ color center laser with different intracavity etalons.
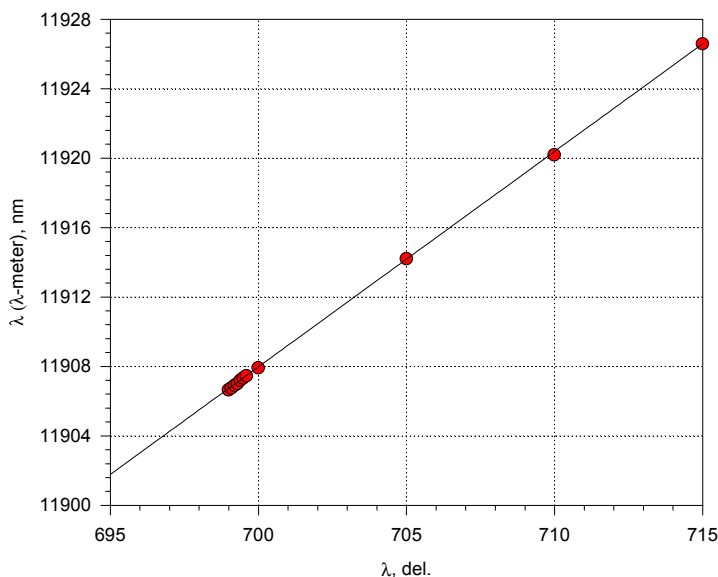
As can be seen from the table the Fabry-Perot interferometer with 60% reflectivity ensured 3 times narrowing of the laser linewidth with sufficiently high output energy. Further

increase of the Fabry-Perot etalon reflectivity improved the output laser linewidth but was accompanied by sufficient drop in the output pulse energy.

The applied construction of the retroreflector mechanism which ensures the simultaneous rotation of the grating and special reflecting mirror and realizes the sinusoidal rotation law of tuning mechanism allowed to obtain linear tuning within the whole range and negligible shift of the laser output beam, which was of great importance for further gas cell pumping experiments. The wavelength of the laser was controlled by the special λ-meter LRL005, connected to the PC. The calibration curve of the laser is shown in Fig. 3.4 demonstrating the linearity of the tuning mechanism.

3.2. High overtone molecular gas pumping experiments.

The designed tunable laser was used to measure the absorption within HCl filled 65 cm long gas cell. The output radiation of the CC laser was focused inside the cell by the lens with 50 cm focal length. The gas cell transmittance was monitored using a pyroelectric detector and TDS-320 digital oscilloscope. The measured absorption spectra of the cell for two HCl gas high overtone absorption lines is shown in Fig. 3.5(a). The Fig. 3.5(b) demonstrates the position of the gas absorption lines according to "Hitran" data. As can be seen from Fig. 3.5(a) the absorption at most intensive line (λ=1190.8 nm) in 65 cm long cell was measured to be about 15% at HCl gas pressure of 400 Torr.
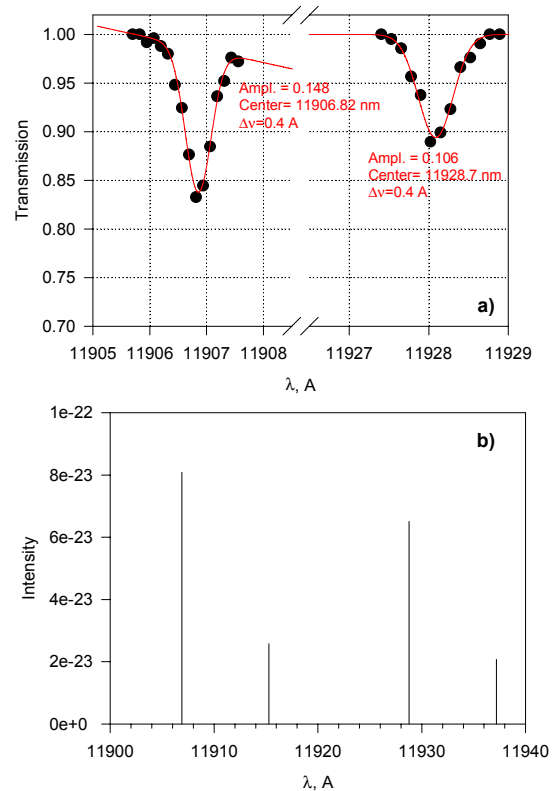

fig. 3. 5 Transmission spectra of the gas cell measured by tunable narrowline CC LiF:F$_2^-$ laser without intracavity etalon (filled dots (a)) and with 60% reflectivity intracavity etalon (empty dots (a)). Solid lines in (a) are gaussian fit of the measured data. Reference HCl absorption lines following "Hitran" (b).

4.   Oscillations of HCl (3-0) molecular gas laser with color-center laser pumping

As was mentioned previously the smooth tuning of the CC laser with two spectra selective elements within the laser resonator was rather a challenge. Though the program modification together with experimental optimization allowed to solve the problem and obtain smooth scanning within 1 nm spectral interval. The computer control was optimized to obtain simultaneous scan of both the grating and intracavity etalon in such a way that after several rotational steps of the intracavity etalon the grating angle was adjusted to keep the optimal relation. The process of the optimization can be illustrated by Fig. 4.1 where scanning using optimal and non o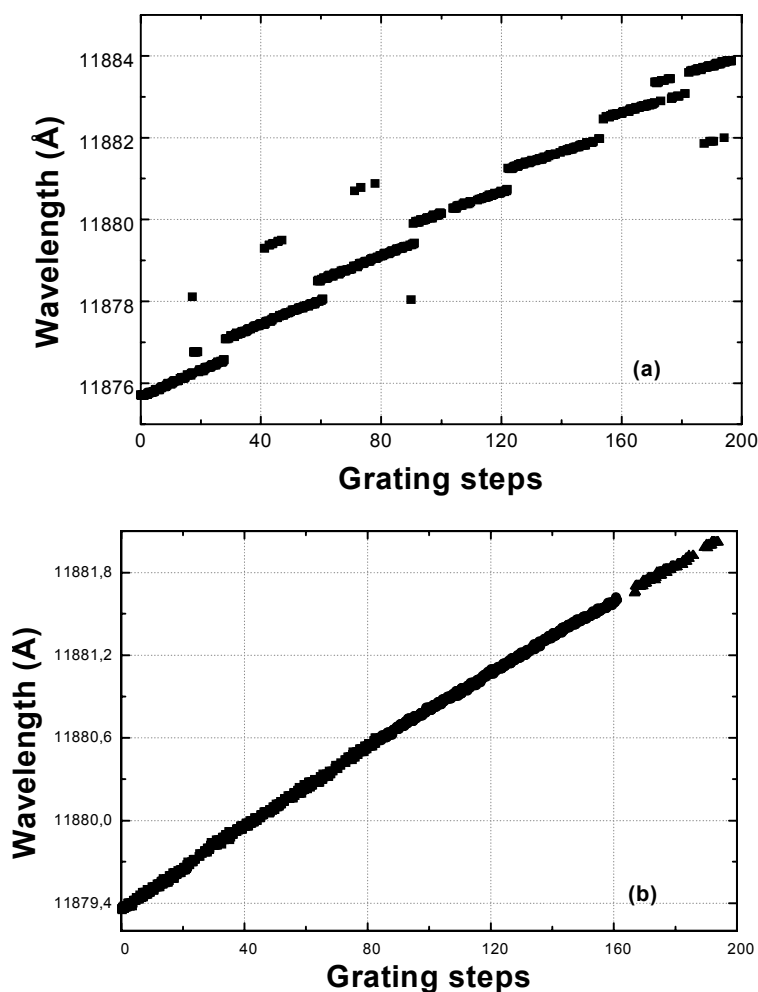ptimal etalon to grating step relation is demonstrated. The wavelength of the laser output was continuously controlled by the wavelength meter based on four Fizo interferometers. As can be seen from the Fig. 4.1 in case of non optimal relation the wavelength of the CC laser changed stepwise, which is absolutely unacceptable in case of precise narrow line measurements. Once adjusted the CC laser computer control can be used further without additional alignment, though it requires that no manual interference in its operation

Fig. 4. 1 Examples of non-optimized (a) and optimized (b) computer controlled scan of the narrowline LiF:F$_2^-$ laser with simultaneous rotation of intracavity etalon and diffraction grating.

presents. This made us to modify the computer program to make all the necessary laser controls automatic (forward and backward scan, returning to initial wavelength position etc). The further attempts to observe the HCl molecular gas absorption revealed some additional problems to be solved. Very narrow gas absorption lines require very stable spectral output of the CC laser. Our numerous measurements showed that the applied scheme need some modifications to support extra high stability for molecular gas pumping. That's why the scheme of CC oscillator was rebuilt to increase the spectral stability.

As was determined by our

Fig. 4. 2 Spectral (a) and amplitude stability (b)of the narrowline LiF:F_2^- laser.

previous investigations the spectral stability is increased when stronger focusing inside the CC crystal is used. The focusing was experimentally optimized, but some spectral instability was still observed. The cause of such instability was determined to be the Brewster shape of the CC laser active element, which resulted in principally noncollinear paths of the pump and oscillating beams outside the element due to wavelength dispersion. Such noncollinearity converts all the space instabilities of pump radiation into output wavelength variations due to small changes in the path angle. To avoid the problem the Brewster cut active element was replaced with another one with perpendicular antireflection coated faces. Additionally the length of the element was shortened to decrease the optical resonator length, which also positively effected the output wavelength stability. As a result the output spectral and amplitude stability were sufficiently improved, which can be illustrated by Fig. 4.2. As can be seen from the Fig. 4.2 some further temperature stabilization is required as the laser spectral stability increases after several minutes
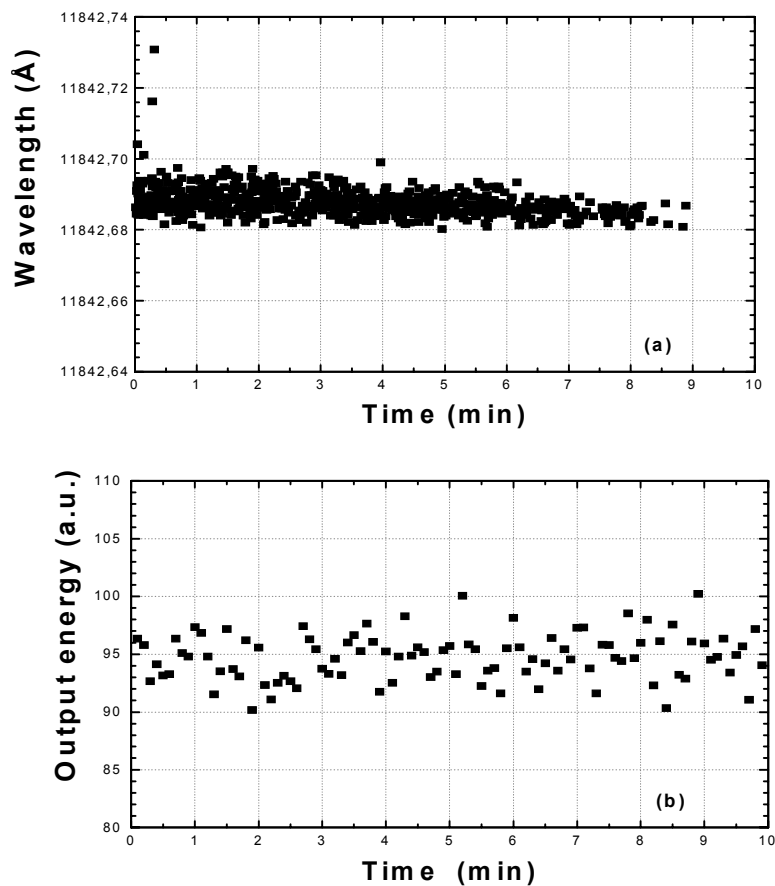
of operation due to achievement of some temperature equilibrium. The linewidth of the laser output was measured using the most precision Fizo interferometer of the wavelength meter equipped with CCD array. The resulting measurements are shown in Fig. 4.3. As one can see the linewidth of about 0.01 cm^{-1} is readily achieved. This modified oscillator was used together with the CC amplifier in further experiments for HCl

Fig. 4. 3 Oscillation linewidth of the narrowline LiF:F$_2^-$ laser measured by Fizo interferometer and CCD array.

molecular gas pumping. The system output pulse energy was about 30 mJ with total efficiency of about 25% relative to YLiF$_4$:Nd laser pump.
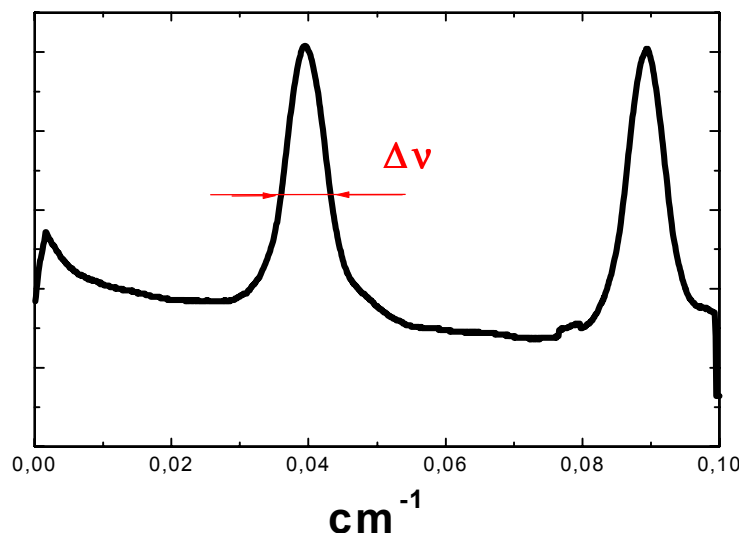
Analogous to previous experiments with HF molecular gas the absorption in 65 cm long cell was measured to define the precise position of molecular gas absorption lines. As the scanning range was very wide the etalon was temporary removed from the scheme and the scan was performed by grating rotation. The linewidth of the laser increased up to 0.3-0.4 cm^{-1}, but the tuning range was wide enough to observe precisely two HCl molecular gas absorption lines as can be seen in Fig. 4.4. The gas pressure in the tube was rather large (about 350 Torr) to make the
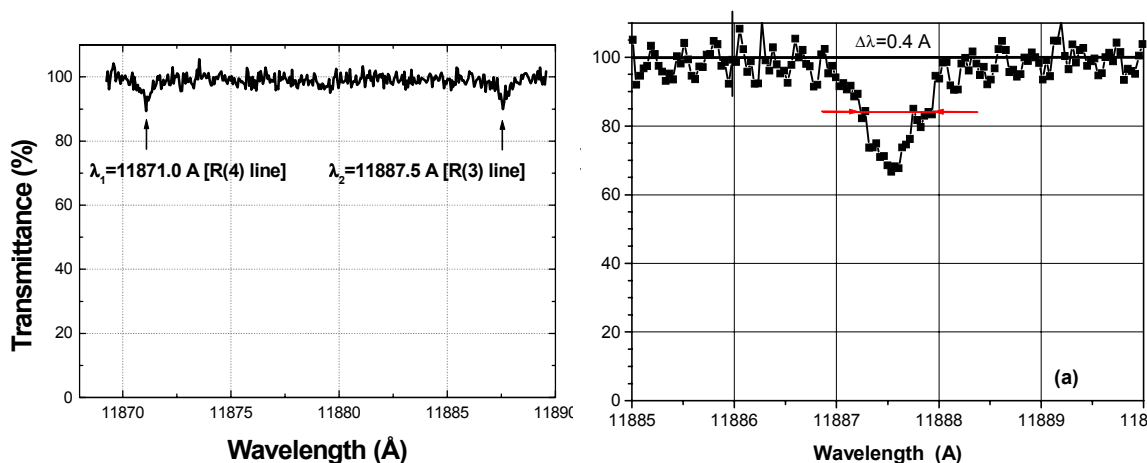

Fig. 4. 4 Absorption lines of HCl molecular gas measured by scanning of LiF:F$_2^-$ laser with removed intracavity etalon ($\Delta\nu_{osc}$=0.3-0.4 cm^{-1}).

absorption observations easier. When the absorption lines were observed the intracavity etalon was returned back to its place and single absorption line was scanned by narrow line pump.

To increase the measurements sensitivity three passes through the gas cell were applied. The resulting absorption line shape is demonstrated in Fig. 4.5. As can be seen from the Fig. 4.6 the absorption line has not become

Fig. 4. 6 The shape of the R(3) HCl molecular gas absorption line at 350 Torr pressure scanned by LiF:F$_2^-$ laser without (a) and with (b) intracavity etalon ($\Delta\nu_{osc}$=0.008-0.01 cm^{-1}).

narrower despite approximately the order of magnitude narrower laser linewidth. That means that the absorption line shape is completely determined by the width of the molecular gas absorption line at 350 Torr pressure.

Unlike previous measurements with HF molecular gas the gas cell was modified and according to our request additionally equipped with liquid nitrogen cooled gas trap, which allowed to decrease rather easily the gas pressure in the cell without realignment of the optical scheme. Using this liquid nitrogen cooled trap, the pressure inside the gas cell was decreased approximately by the order of magnitude and the scan by narrow line laser was repeated. The pressure decrease resulted in sufficient narrowing of the absorption spectra as can be seen in Fig. 4.6. When the absorption line position was precisely determined the gas tube was refilled to achieve the maximum
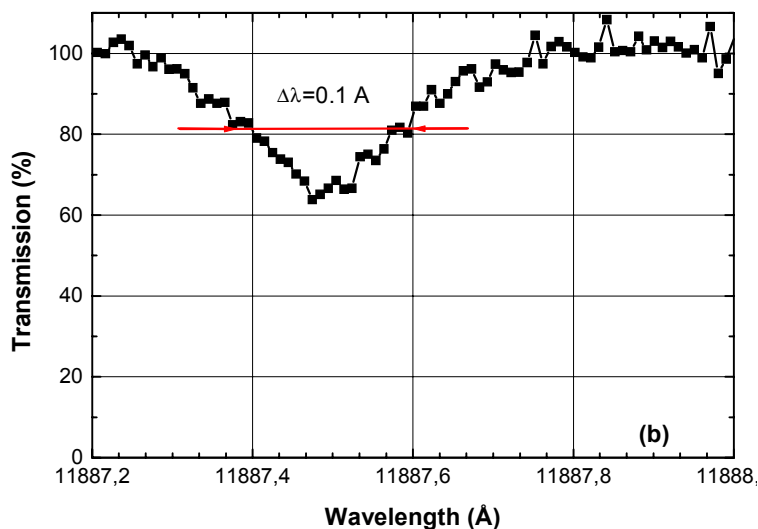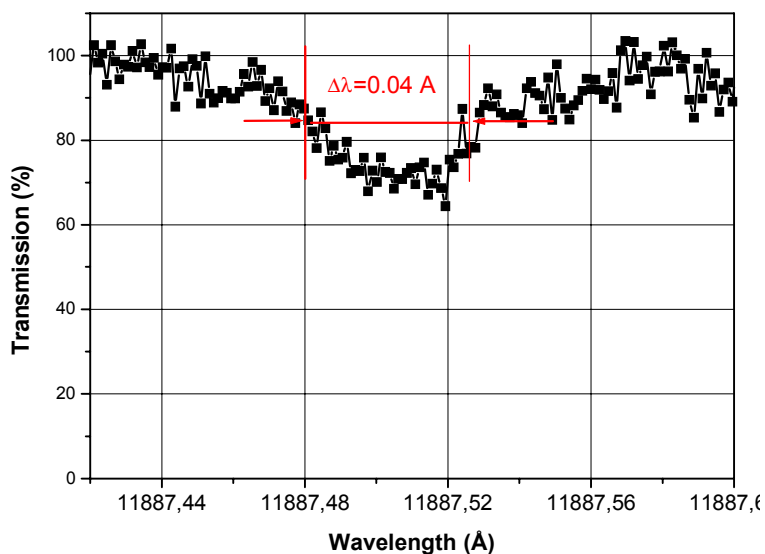

Fig. 4. 5 The shape of the R(3) HCl molecular gas absorption line at approx. 30 Torr pressure scanned by narrowline LiF:F$_2^-$ laser.

pressure of approximately 20 Torr. Again liquid nitrogen cooled gas trap allowed us to change the pressure during the experiments.

Fig. 4. 8 Reflectivity spectra of the HCl molecular gas laser cavity mirrors.

To observe the HCl molecular gas oscillations the pumping scheme was rebuilt to obtain single pass of pump radiation through the gas cell and two mirrors were placed to form the laser cavity. The backward mirror was curved one with curvature radius of 10 m and the output mirror was flat. The reflectivity spectra of the mirrors used in the experiment are shown in Fig. 4.7. The pump beam diameter was about 5 mm and no focusing inside the gas cell was applied. When the HCl molecular gas cavity was aligned the pump laser was slowly tuned near the maximum of absorption spectra and the gas laser output was continuously controlled by liquid nitrogen cooled Ge:Au photodetector.

The resulting dependence of HCl molecular gas output on CC laser pumping wavelength is demonstrated in Fig. 4.8. The double peak shape of the measured curve is the result of small misalignment of the narrowline LiF:F$_2^-$ pump laser leading to simultaneous lasing of two longitudinal modes. To determine the HCl molecular gas oscillation wavelength the laser output was sent to the B&M Spectronic 25 cm grating monocromator with liquid nitrogen cooled Ge:Au photodetector. The measured oscillating wavelength was measured to be λ=3.881±0.004 μm

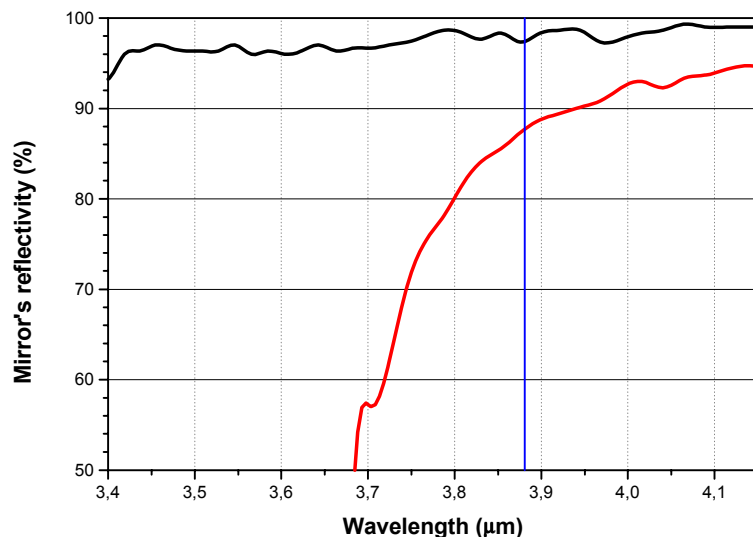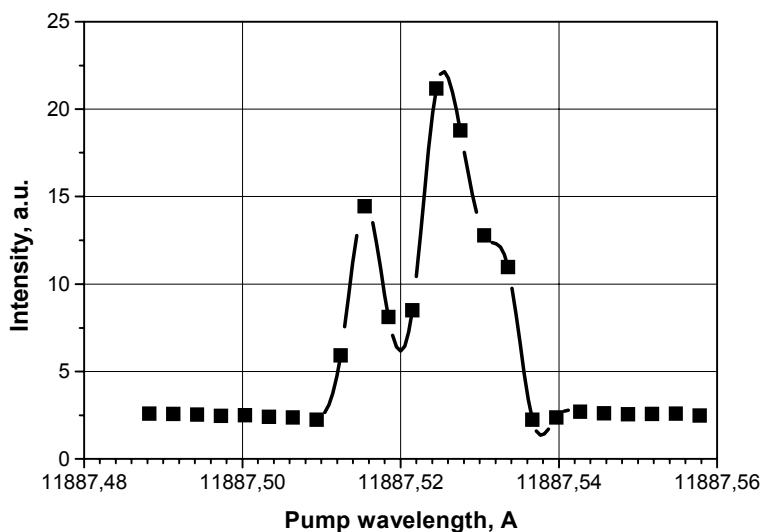*Fig. 4. 7 The lasing output of P(5) HCl molecular gas laser line with narrowline LiF:F$_2^-$ laser scanned near the maximum of absorption line.*

which corresponds to 3→2 transition of P(5) HCl molecular gas line.

To measure the input-output characteristics of the HCl molecular gas laser a set of neutral filters was applied which allowed stepwise change of the pump pulse energy. For precise measurements the amplitude of both input and output signals was controlled by fast Ge pin photodiode (pump) and liquid nitrogen cooled Ge:Au photodetector (HCl laser oscillations). Measured oscillograms of pump and

Fig. 4. 9 Oscillograms of narrowline LiF:F$_2^-$ pump and P(5) HCl (3-2) molecular gas oscillating pulses.

oscillation pulses can be seen in Fig. 4.9. As can be seen from the Fig. 4.9 the delay (τ_{del}) between the pump and the lasing pulses is rather short and was measured to be about 50 ns. When pump energy was decreased approximately by 30% by applying the neutral filter the delay between the pump and oscillating pulses increased to about 75 ns. The resulting dependence of HCl laser output on absorbed pump energy is shown in Fig. 4.10. As can be seen from the Fig. 4.10 the slope efficiency of the molecular gas oscillation is about 2%.

In further experiments some focusing of pump radiation inside the gas cell was applied to optimize the pumping intensity. The output beam of narrowline LiF:F$_2^-$ CC laser was focused by 1m focal length lens to achieve rather small pump spot inside the gas cell. The applying of focusing lens arose some additional problems due to focusing of the remaining part of 1.047 mm pump which was earlier spatially separated (due to small output angle difference) to the incidence window of the gas cell.
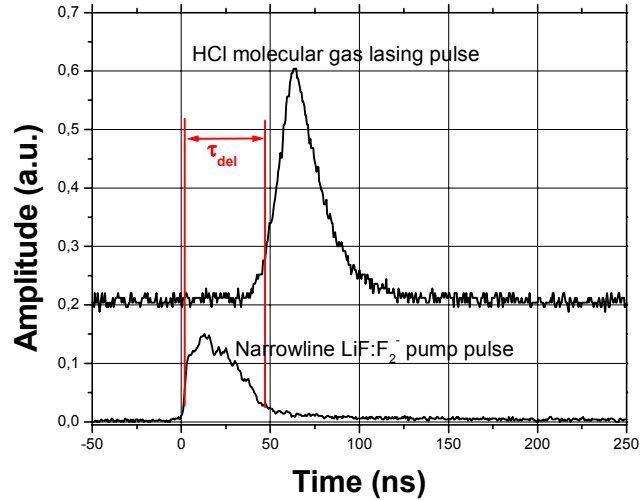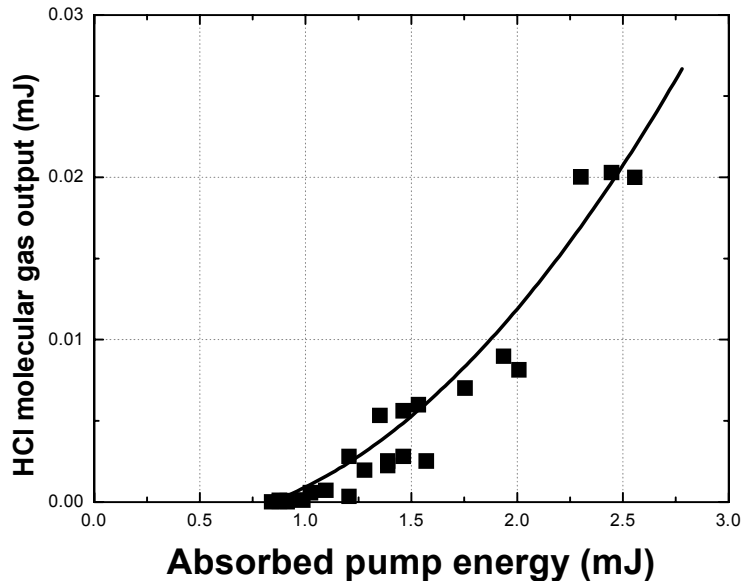

Fig. 4. 10 Input-output characteristics of P(5) HCl (3-2) molecular gas laser.

To avoid such undesirable focusing the special diaphragm was placed at the output of the LiF:F$_2^-$ CC amplifier to obtain additional spatial selection. Though this diaphragm also resulted in some decrease of the maximum incidence pump energy. As the result of such pump intensity increase the lasing energy threshold decreased approximately twice, stability of the HCl molecular gas was sufficiently improved and oscillations could be obtained easier than in case when no focusing inside the gas cell was applied.

Visually the form of the oscillating pulse at the TDS-380 oscilloscope was characterized by modified pulse shape with two distinguishable maximums as can be seen in Fig. 4.11. Such pulse shape can be explained by achievement of oscillation threshold of another HCl molecular gas transition with larger threshold resulting in approximately twice longer delay between the pump LiF:F$_2^-$ and oscillating pulses. To control this statement the spectral output of HCl molecular gas was measured using B&M Spectronic 25 cm grating monochromator and Ge:Au liquid
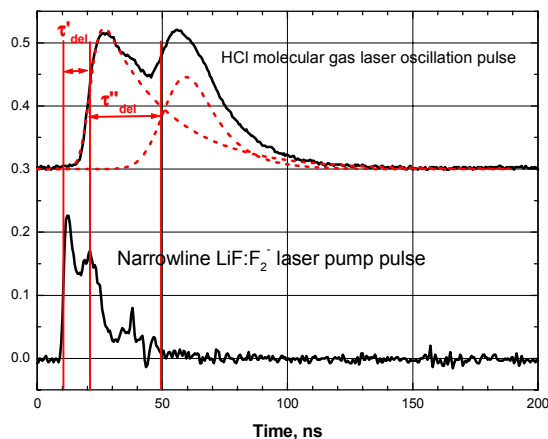

Fig. 4. 11 Oscillograms of the narrowline LiF:F$_2^-$ laser pump pulse and P(5) line HCl molecular gas oscillation pulse with clearly distinguishable double peak structure.
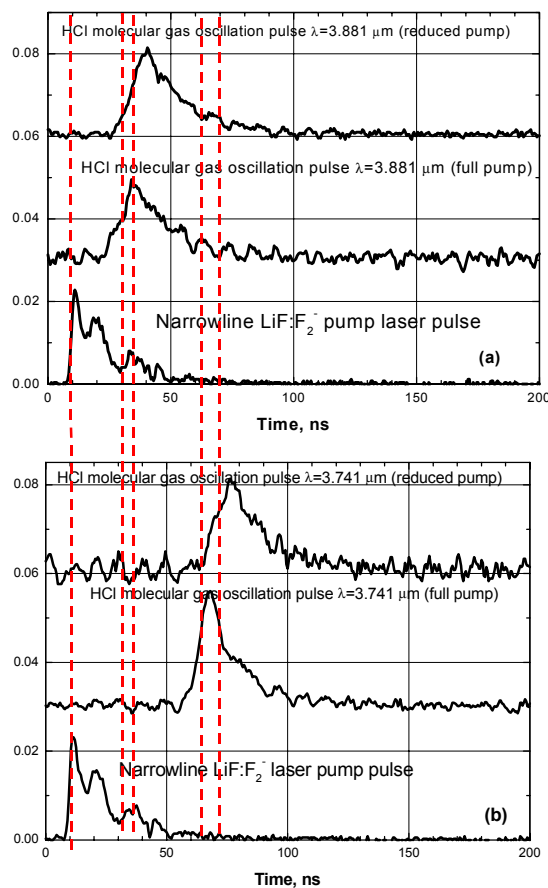

Fig. 4. 12 Oscillograms of narrowline LiF:F$_2^-$ laser pump pulses and HCl molecular gas oscillation pulses at 3-2 (a) and 2-1 (b) transition of P(5) molecular gas line.

nitrogen cooled photodetector. The output lasing spectra was measured to have two oscillating wavelengths $\lambda_1 = 3.881 \pm 0.004$ μm and $\lambda_2 = 3.769 \pm 0.004$ μm which corresponds to 3-2 P(5) and 2-1 P(6) vibronic transitions of HCl molecular gas. That means that the threshold for cascade 3-2; 2-1 oscillations was achieved. The oscillograms of pump and oscillating pulses for two values of pump energy are shown for both oscillating wavelengths in Figs. 4.12(a) and (b). The decrease of pump energy obtained using neutral filter was about 30%. The necessity to place the monochromator lead to increase of the optical path to Ge:Au liquid nitrogen cooled photodetector which resulted in the growth of the absolute value of measured delay time. As can be seen from Fig. 4.12 in both cases the delay between pump and oscillation pulses increases nearly proportional for both oscillating wavelengths when pump energy decreases and the absolute delay values for main 3-2 (τ'_{del}) and cascade 2-1 (τ''_{del}) oscillations were close. Comparing with the case when no focusing was applied one can mention sufficient (approximately 5 times) shortening of the delay between the pump pulse and the pulse of 3-2 HCl molecular gas oscillations.

Using stepwise decrease of incidence pump energy by a set of neutral filters the input-output characteristics of HCl molecular gas laser were measured. Additionally the delay between the pump and oscillating pulses was controlled. The resulting graphs are shown in Figs. 4.13 (a) and (b).
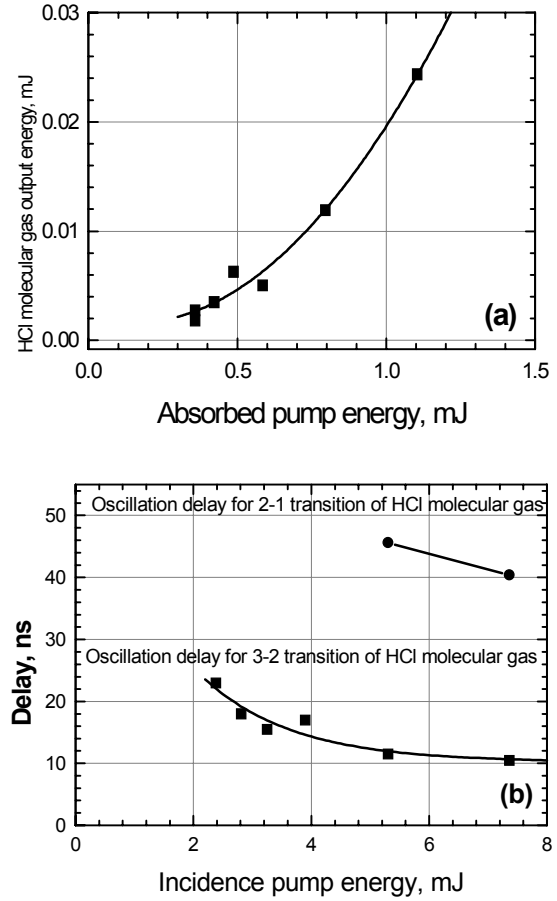

Fig. 4. 13 Input-output characteristics of P(5) line of HCl molecular gas laser (a) and delay time between the narrowline LiF:F_2^- pump pulse and oscillation pulse of 3-2 and 2-1 transition of HCl P(5) molecular gas line (b).
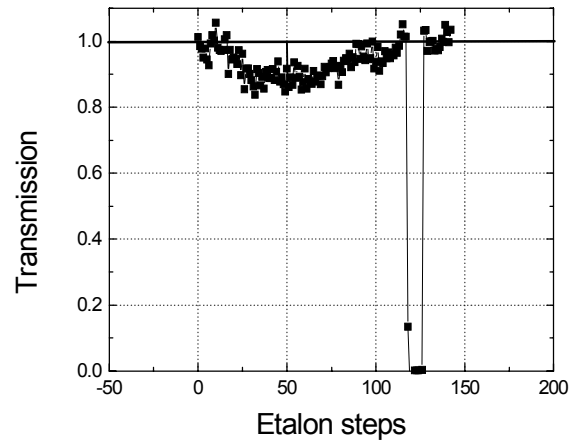

Fig. 4. 14 Scan of the HCl molecular gas absorption line by smooth tuning of LiF:F_2^- narrowline laser

As can be seen from Fig. 4.13(a) laser slope efficiency increased twice till 4% under some focusing conditions. Such a small value of slope efficiency together with short build up time (which demonstrates high gain in molecular gas cell) can be explained by high output coupling and quite high round trip intracavity losses in our cell. To evaluate the part of absorbed pump energy the absorption in the gas cell was measured using piroelectric photodetector by scanning the wavelength of LiF:F_2^- narrowline CC laser and fully aligned HCl molecular gas laser cavity. The resulting scan is shown in Fig. 4.14. As one can see from the Fig. 4.14 the absorbed energy in the maximum of absorption line is only about 15%.

Conclusions

The parameters of narrowline LiF:F_2^- laser pumping were optimized and cascade oscillations at the (3-2) P(5) transition (wavelength 3.881±0.004 μm) and at the (2-1) P(6) transition (3.769±0.004 μm) of HCl (3-0) molecular gas laser with slope efficiency of about 4% relatively to absorbed pump energy was obtained. The delay time between HCl molecular gas oscillation pulse and LiF:F_2^- pump pulse at both oscillating cascades was measured for different pumping intensities.